THE HYSTERESIS MOTOR

by

George Nagy

A thesis submitted to the Faculty of
Graduate Studies and Research in partial
fulfilment of the requirements for the
degree of Master of Engineering.

Department of Electrical Engineering
McGill University
Montreal.

August 1960

SUMMARY

Significant contributions to the theory of the hysteresis motor are briefly reviewed, and certain shortcomings of the present theory indicated. A novel approach to calculating the asynchronous torque, based on a surface integral instead of the customary volume integral, is presented.

An experimental hysteresis motor, and several methods of testing the theory, are described, and deviations from the predicted performance examined with a view to establishing the magnitude of the various losses. Evidence is advanced to show that subsidiary loops in the hysteresis curve are not the major cause of inefficiency, and that laminating the rotor improves the efficiency considerably by eliminating large, tooth-frequency eddy current losses.

Synchronous performance and the effects of remanent magnetism are analyzed with the help of vector diagrams, and the notable increase in efficiency on pulsing the motor is explained in similar terms.

Some design principles and possible applications are suggested for the larger hysteresis motors now in prospect.

ACKNOWLEDGEMENTS

The subject matter of this thesis, as well as the principal lines of approach, were suggested by Dr. T. H. Barton. His patient and understanding guidance sustained the project through many an apparent impasse.

The author also wishes to extend his gratitude to the rest of the Electrical Engineering Department, Professors and Graduate Students, who were never too busy to explain the vagaries of some particular piece of apparatus or to lend a ready hand with the more intricate measurements. Special mention is due to the Technicians of the Department for their help in constructing the experimental hysteresis motor.

Finally, the author is deeply indebted to the National Research Council whose interest and financial support made the project possible.

TABLE OF CONTENTS

LIST OF FIGURES

LIST OF TABLES

CHAPTER I

Operating Principles

1.1 Introduction.

The application of the phenomenon of hysteresis to the conversion of electrical energy to mechanical power through the medium of the magnetic field has been known and exploited for well-nigh sixty years. Despite this, classical treatises on alternating current machinery rarely go beyond a cursory description of the hysteresis motor; more recent works avoid it altogether since the essential non-linearity of the hysteresis process does not readily lend itself to the methods of Unified Machine Theory and matrix, albeit tensor, notation.

Advances in metallurgy within the last ten years have resulted in alloys with magnetic and physical properties favourable to the construction of hysteresis motors capable of more efficient operation than hitherto thought possible. The topical interest thus enjoyed by the hysteresis motor seems to present an opportune occasion to reassess and test existing theories about its operation, and to probe further into the nature of the secondary phenomena influencing its performance. This investigation constitutes the primary purpose of the present research project.

In its simplest form, the hysteresis motor comprises a stator, appropriately wound and excited to provide the components of a rotating magnetic field, and a rotor, consisting in whole or in part of ferromagnetic material. The interaction of the flux induced in the rotor with the magnetomotive force producing it provides the torque; this process will be examined in greater detail in the following sections.

It is important to note that the above description of the hysteresis motor applies equally well to the solid rotor induction motor. It is therefore necessary to ensure that experimentally the hysteretic behaviour is separated from the effects of the circulating currents; this is most easily accomplished by laminating the rotor. Previous investigators were handicapped by the lack of high loss hysteresis materials in sheet form, and their results necessarily reflect the effects of eddy currents.

As with most electromagnetic phenomena, several explanations of the modus operandi of the hysteresis motor are available. One new treatment and several older ones will be briefly described in the next five sections.

1.2 Interaction of M.M.F. and Flux at Rotor Surface.

Though to the author's knowledge the surface integral method - a method gaining in popularity[1] - has not yet been applied to the analysis of the hysteresis motor, it offers perhaps the greatest insight to the torque producing process. Since the interior of the rotor is assumed homogeneous, a particularly simple approach is practicable.

For the purpose of illustration, let an extremely simple model (Fig. 1.1) consist of the plane boundary of two semi-infinite slabs, one fixed and of infinite permeability, the other free to move and of hysteretic material. A sinusoidally distributed current sheet J, moving parallel to the boundary at linear velocity v, produces a magnetomotive force H with normal and tangential components H_n and H_t (Maxwell's equations imply that if a sinusoidally varying H exists perpendicular to the interface, a sinusoidally varying component must also exist parallel to the interface and perpendicular to J) which in turn induces a flux density B perpendicular (and also parallel) to the interface.

STATOR

$Jx = Jy = 0$

$Jz = J \sin\left(\frac{x}{\lambda} - \omega t\right)$

$\mu = \mu_s e^{-j\alpha_1}$

$\mu_s = \infty$

$\alpha_1 = 0$

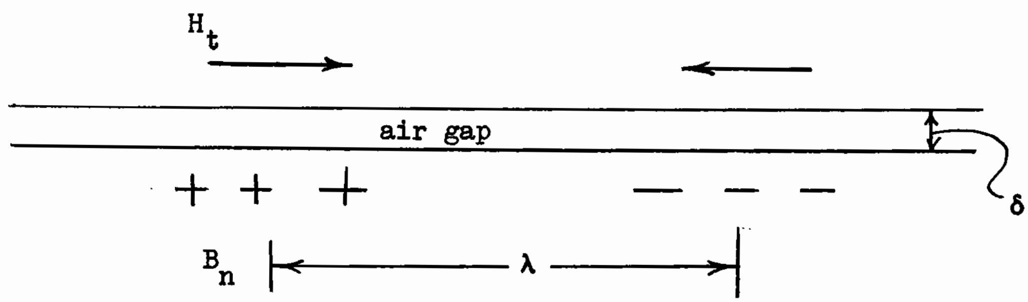

0

ROTOR

$\mu = \mu_r e^{-j\alpha_2}$

$\mu_r = \mu_r$

$\alpha_2 = \alpha$

Fig. 1.1 Plane Model of Hysteresis Motor

On the fixed (stator) side of the boundary, the corresponding magnitudes of H and B always occupy the same position in space, and the only force on the stator is that experienced by the current sheet. In the movable slab (rotor), however, H and B are not in phase, and the reaction between them $(\overline{H} \times \overline{B})$ produces a force on the face of the rotor.

To adopt an even more unsophisticated point of view, H induces a magnetic pole density corresponding to the discontinuity in B_n on the surfaces, which in the rotor is not, due to hysteresis, identically distributed with the m.m.f. causing it. Since these poles lie in a magnetic field with both tangential and normal components, they experience tangential and normal forces in accordance with the elementary laws of magnetism. The normal force cannot produce motion, while the tangential force will attempt to accelerate the rotor in the direction of the motion of the field until the induced poles overtake the m.m.f. wave.

Fig. 1.2 shows the current, m.m.f. and flux density (or surface pole density) on both sides of the interface. Since the flux density and m.m.f. in the rotor are related to one another by the hysteresis loop of the material, B in general cannot be sinusoidal if H is. Thus the sinusoidal distributions shown in Fig. 1.2 represent only the fundamental components. The hysteretic angle of lag, which along with the permeability characterises ferromagnetic materials, is a measure of the retardation of the fundamental of B, since the maxima of H and B perforce coincide.

If the rotor is moved by an external force at a velocity superior to that of the current sheet, then the electric field generated at the interface by the flux from the rotor leads the current by more than 90°, and the direction of the power flow is reversed. This does not, in general, constitute an economical method of generating electricity, since an alternating source must already be available to set up J.

While the model described in this section illustrates the essential features of the hysteresis motor, quantitative results which may be tested by experiment can hardly be deduced. In Chapter II, a cylindrical model, bearing closer resemblance to the real motor, will be proposed, and the pertinent equations solved.

1.3 The Conservation of Energy-Steinmetz.

Steinmetz[2], the first to give a quantitative treatment of the hysteresis motor, applied the universal "power balance" method to the problem. His model consists of an iron disk in a rotating magnetic field.

Let f = supply frequency

V = volume of iron in the rotor

η = coefficient of hysteresis

B = magnetic density (flux density)

$$J_z = -J \sin\left(\frac{x}{\lambda} - \omega t\right), \quad x = 0$$

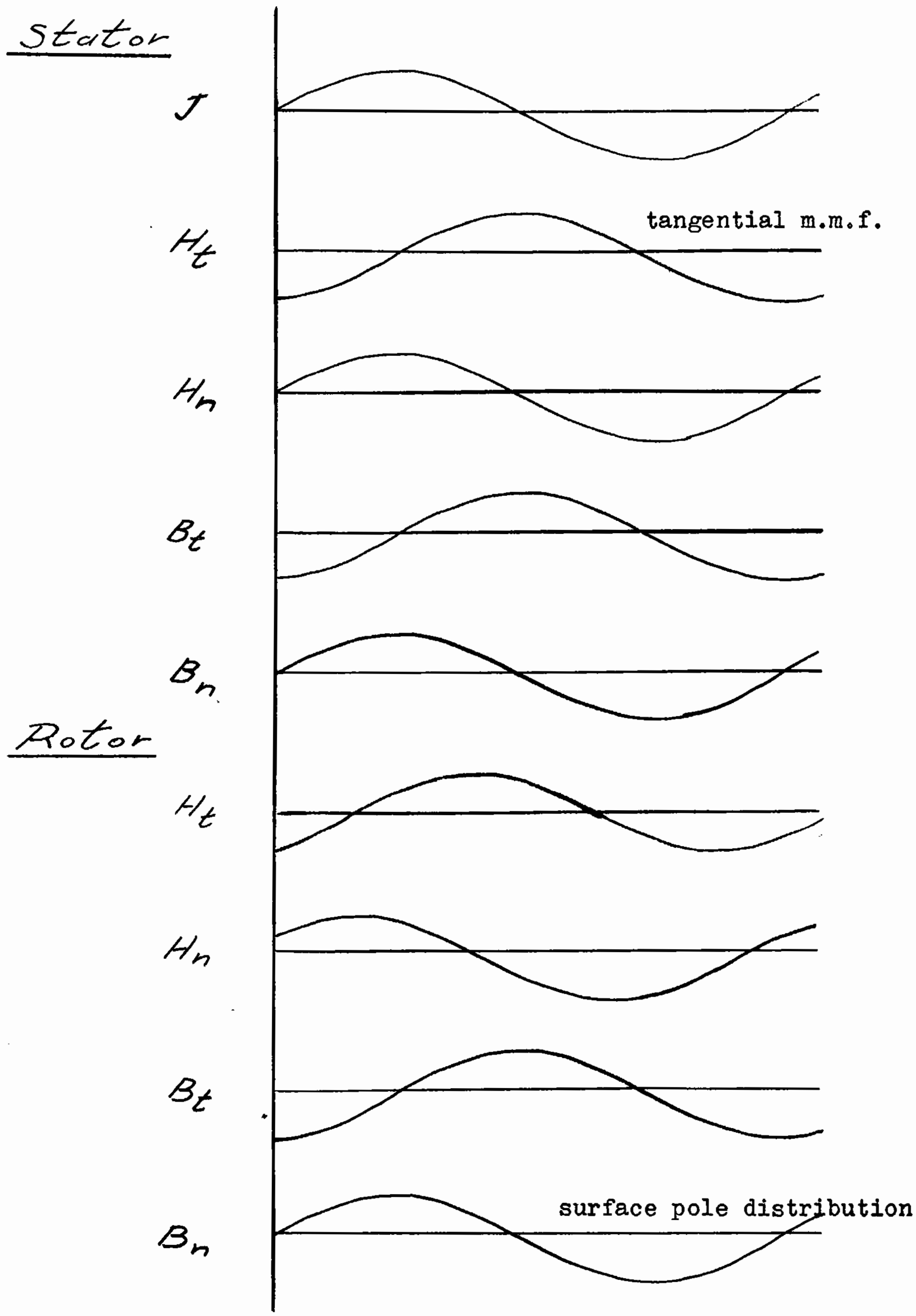

Fig. 1.2 Current, Flux and M.M.F. Distribution in Plane Model.

Then the energy lost per cycle is $V\eta B^{1.6}$ and the power supplied to the stator, $P_o = fV\eta B^{1.6}$, since the power input is evidently independent of the speed as long as the reluctance of the magnetic circuit containing the rotor, and hence the current, is constant.

The rotor, however, sees a field rotating at a speed proportional to the slip s, and the loss in the rotor is $P_1 = sfV\eta B^{1.6}$.

Thus in the transfer from the stator to the rotor an amount of power equal to $P = P_o - P_1 = (1-s)fV\eta B^{1.6}$ has disappeared, and must be available as work at the shaft. The torque is $T = \frac{P}{2\pi f/p\ (1-s)} = \frac{pV\eta B^{1.6}}{2\pi}$, independent of the speed.

$\eta B^{1.6}$ merely represents the energy loss per cycle per unit volume of rotor material. Hence Steinmetz's expression is equivalent to $T = \frac{p}{2\pi} VA$, where A is the average area of the hysteresis loop.

It may be noted in passing that the Steinmetz exponent for modern materials is higher than 1.6, and is usually in the region 1.9 to 2.0.

Steinmetz was also the first to differentiate clearly between hysteresis, the double valued relationship between H and B, and what he termed "molecular friction", i.e., the transformation of electromagnetic energy into heat; he states that these are identical only if there is no other source or sink of power in the magnetic circuit. This distinction is one well worth keeping in mind.

1.4 Virtual Work - Teare.

In 1939, B.R. Teare, Jr., published a paper[3] on a theoretical and experimental investigation of the hysteresis motor. He chose to treat a rotor consisting of a thin cylindrical shell, a most economical design producing maximum torque per unit weight of high loss material.

Teare bases his derivation for the resultant torque on the virtual work equation:

$$T\delta\theta = -\delta W$$

where $\delta\theta$ = virtual displacement

δW = virtual work

The first step is the calculation of dW for a volume element dV of the rotor; this is equivalent to the product of the flux density due to the stator and the intensity of magnetization.

Several assumptions are now introduced (the tangential components of $\overline{B}$ and $\overline{H}$ are neglected, and average values replace integrals) and finally the torque is calculated on the basis of an elliptical hysteresis loop. While the theoretical results are shown not to deviate too markedly from the experimental ones, most of the approximations hold only for motors of dimensions similar to Teare's.

Teare points out that harmonics moving with the fundamental frequency have little effect on the torque, but those moving relative to it give rise to subsidiary loops which reduce the area of the main loop, and hence the torque.

Teare's paper serves as an excellent illustration both of the power and of the complexity of the virtual work principle.

1.5 Loop Energy Method - Roters.

Roters' paper[4] does not delve deeply into the actual mechanism of the torque production, and his development of the torque equation essentially duplicates that of Steinmetz.

The total loss of the rotor per pair of poles slipped by is $W = V \oint H dB$ where the symbols have their previous meaning. Since the energy loss is transmitted through the agency of the magnetic field, as a torque times the speed of the field, the hysteresis power developed in the rotor will be:

$$P = fV \oint HdB$$

and the torque

$$T = \frac{fV \oint HdB}{2\pi n} \quad \text{where } n \text{ is the rotational speed of the stator field in r.p.s.} = f/p$$

$$= \frac{pVA}{2\pi}$$

Here, as in Section 1.4, it would be more exact to write

$$T = \frac{p}{2\pi} \int_V \left[\oint \overline{H} d\overline{B} \right] dV \quad ,$$

since the average value of the various loop areas traced out in different parts of the rotor is required. Thus the flux distribution inside the rotor must be known in order to predict the torque.

Roters principal concern is the reduction of the parasitic losses already mentioned in Teare's paper. He advocates the construction of closed slot stators in order to reduce the variations in the air gap flux. Unfortunately, the magnitude and method of measurement of the losses is not discussed, although considerable experimental data does seem to show that the closing of the slots does indeed improve performance. It will be shown in Chapters IV and V that the magnitude of the parisitic losses does not constitute a primary problem, and that efficiencies comparable to that of induction motors may be obtained with ordinary stator construction. It is to be noted however, that Roters used essentially thin shell, unlaminated rotor construction, where high frequency losses due to subsidiary loops, and especially those due to eddy current, would be relatively very much greater.

An improvement entailing fewer disadvantages than the closing of the slots is also suggested by Roters: momentarily overexciting the stator at synchronism by about 80% in order to permanently magnetize the rotor, thus reducing the exciting current. This too will be discussed in greater detail in Chapter V.

1.6 Larionov, Masteyev, Orbov and Panov.

The above group made the most recent (1958) contribution[5] to the theory of the hysteresis motor. The highly theoretical paper develops a rather complicated equivalent circuit taking into account eddy current effects, and a few experimental results are presented to support the theory. Unlaminated Vicalloy, the material used in laminated form in the present experiment, is employed; it is regrettable that a description of the actual motor tested is not included so that a comparison could be made.

An interesting aside in the article is the theoretical treatment of a motor with the rotor mounted outside the stator. Since the heat dissipated in the rotor is proportional to the slip (1.3) this construction may be practical for a motor customarily operating at a high slip yet capable of synchronous performance. This design, however, would not utilize one of the most advantageous features of the hysteresis motor, namely that no electrical connection to the rotating member need be made.

CHAPTER II

Derivation of the Torque Equation

2.1 Procedure.

Since the hysteresis motor is essentially a constant torque device whose synchronous speed is determined by the stator winding and the applied frequency, any theory attempting to describe hysteresis motor performance must evaluate the torque produced by a given excitation in terms of the stator and rotor parameters. In this chapter the surface integral method outlined in Section 1.2 will be applied to evaluate this torque.

The geometric and magnetic properties of the actual motor tested are unfortunately too complicated to be directly amenable to mathematical treatment; in order to arrive at a solution a model will be proposed and the assumptions involved justified. Section 2.2 discusses in some detail the substitution of an ellipse for the actual hysteresis loop of the stator and rotor, while Section 2.3 describes the physical features of the model in terms of the appropriate boundary conditions.

Once the problem has been thus simplified, the solution is straightforward. Maxwell's equations, now free of the non-linearities inherent in real hysteresis curves, are solved for B and H in Section 2.4 in terms of the boundary conditions developed in 2.3. Then the force on an element of rotor surface is determined, and integration around the periphery yields the total torque. The expression thus derived is shown to be equivalent to that resulting from the energy transfer methods.

It will be seen that the real advantage of the method about to be developed over the customary energy method is that it permits the evaluation of the torque in terms of the loop area measured with an annular sample of the rotor material a.c. magnetized to the maximum value of the air gap flux density. The energy methods are usually based on the actual hysteresis curves, which cannot be conveniently expressed in mathematical terms, and consequently the magnitude of the losses per rotor revolution must be obtained experimentally.

It is, of course, possible to obtain analytic solutions from the energy methods as well by applying the concept of complex impedance, but in the author's opinion this does not lead to as clear a physical picture of the principles underlying the method of operation of the hysteresis motor.

2.2 Elliptical Approximation to the Hysteresis Loop.

It may be seen from Fig. 2.1 that below saturation levels the shape of the hysteresis loop is not too unlike that of an ellipse. The difference is most pronounced at the peak values of H and B, which occur simultaneously in the real loop but lag one another by the angle α in the ellipse. This does not present a major obstacle as far as the derivation of the torque is concerned, since the torque will be shown to be proportional to the total loop area, while the peak region constitutes only a small portion thereof.

The ellipse may also be regarded as a Lissajous pattern formed by two sinewaves of the same frequency and differing in phase by α. This viewpoint makes it convenient to define a complex permeability $\overline{\mu} = |\mu|\ e^{-j\alpha}$. Thus

$$\overline{B} = |\mu|\ e^{-j\alpha}\ \overline{H}$$

has meaning only if H is a periodically varying quantity and a phase difference may exist. If H is sinusoidal, then $H = H_1 e^{-j\omega t} = H_1 \cos \omega t$ and $B = |\mu|\ H_1 e^{-j(\omega t+\alpha)} = B_1 \cos (\omega t+\alpha)$ where H_1, B_1 denote maximum values.

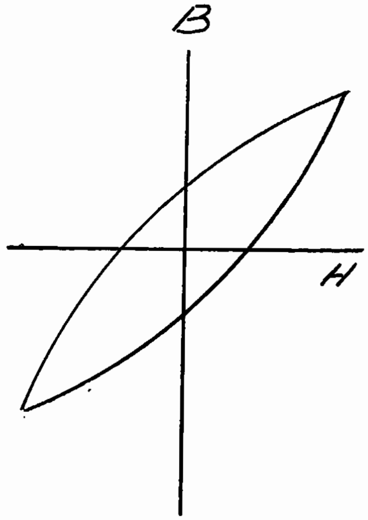

Fig. 2.10a Hysteresis Loop at Low Flux Densities

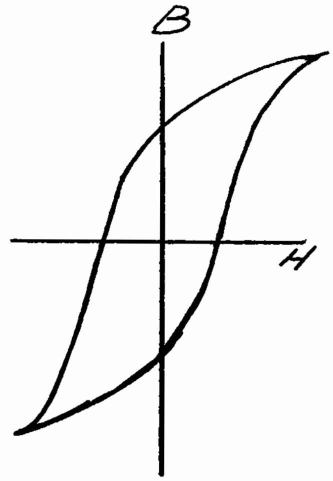

Fig. 2.10b Hysteresis Loop at High Flux Densities

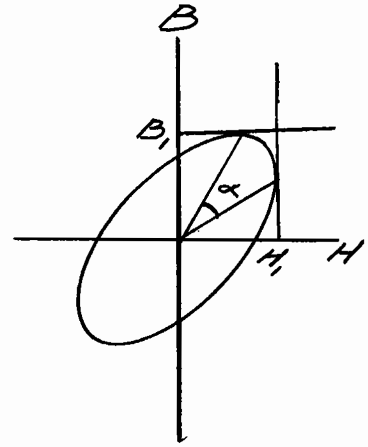

Fig. 2.10c Elliptical Hysteresis Loop

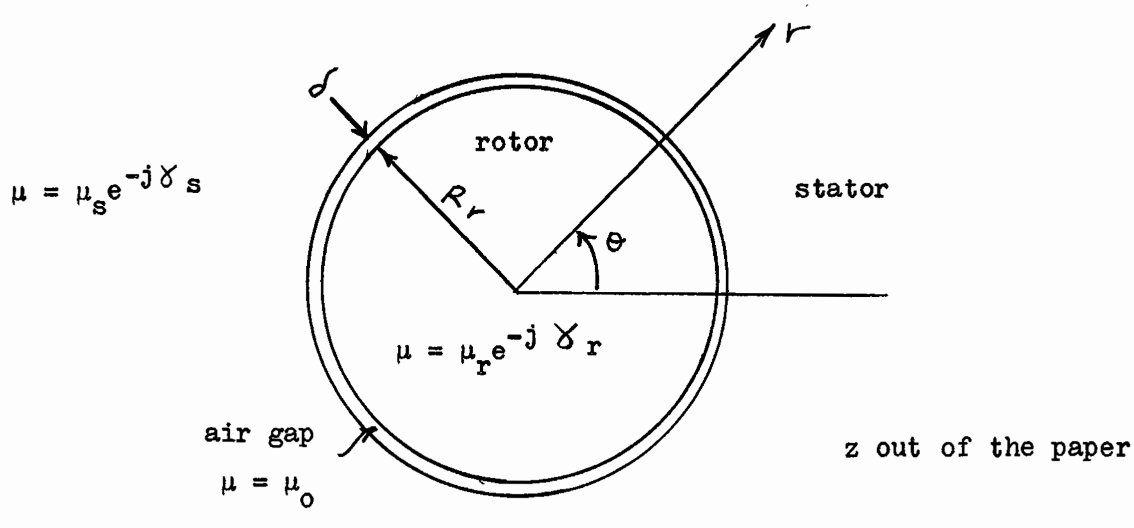

Fig. 2.2 Cylindrical Model of Hysteresis Motor.

In the course of the derivation of the torque formula, the area of the hysteresis ellipse will be required in terms of the maximum values of H and B rather than the major and minor axes. This area will now be calculated by integrating $\int_{-H_1}^{H_1} B\,dH$:

$$B = B_1 \cos(\omega t+\alpha) \quad \text{and} \quad H = H_1 \cos \omega t$$

$$B = B_1 \cos(\omega t+\alpha) = B_1 \left\{\cos \omega t \cos \alpha - \sin \omega t \sin \alpha\right\}$$

$$= B_1 \left[\frac{H}{H_1} \cos \alpha \pm \sqrt{1 - \frac{H^2}{H_1^2}} \sin \alpha\right]$$

$$\text{At } B = 0, \quad H = \pm H_1 \sin \alpha$$

$$\text{Area} = 2\int_{-H_1 \sin\alpha}^{H_1} \frac{B_1}{H_1} \left[H \cos \alpha + \sqrt{H_1^2 - H^2} \sin \alpha\right] dH$$

$$- \int_{+H_1 \sin\alpha}^{H_1} \frac{B_1}{H_1} \left[H \cos \alpha - \sqrt{H_1^2 - H^2} \sin \alpha\right] dH$$

$$= \pi H_1 B_1 \sin \alpha \qquad (2.1)$$

In the real hysteresis loop there is no feature corresponding to α, which assumes physical significance as a phase lead or lag of the fundamental only if either $\overline{H}$ or $\overline{B}$ is quasi-sinusoidal. Consequently, in order to determine α it is necessary to measure the area of the loop, and then to calculate α through equation 2.1 substituting real maximum values for H_1 and B_1. This procedure is rather arbitrary, and was chosen mainly because of its simplicity. A slightly different value would have been reached by considering the maximum values of the fundamental components of H and B. Although the final torque formula may be expressed in terms of the loop area alone, it is important to recall that the surreptious introduction of α in the mathematical manipulation of Maxwell's equations conceals an approximation.

2.3 The Cylindrical Model.

The geometric model will comprise three infinitely long co-axial cylindrical regions, a stator, an air gap, and a rotor, as shown in Fig. 2.2. The permeability of the stator, which extends to infinity in the radial direction, is $\mu_s e^{-j\gamma_s}$, of the rotor, $\mu_r e^{-j\gamma_r}$, and of the air gap, μ_o. A sinusoidal current sheet $\bar{J}$ pointing in the z-direction is affixed to the stator-air gap interface, and moves forward in the positive θ-direction at angular velocity ω, where $\omega = \frac{2\pi f}{p}$ is the angular frequency of the supply and p is the number of pole pairs. The conductivity at the stator surface is infinity, and zero everywhere else.

The above model introduces the following approximations with respect to the real motor (Chapter III):

a. End effects are neglected. This is more serious than in a similar treatment of induction motors, because the permeability of the rotor is only about fifteen times that of the air gap, and consequently leakage fluxes may be significant.

b. The shaft of the rotor, of mild steel, has very high permeability compared to the rest of the rotor. It will be seen however that except in the case of the two pole stator, the flux densities at the center are very low. In any case, the addition of a fourth layer to the model would not in principle make the problem more difficult to solve.

c. The finite dimensions of the stator may raise the reluctance of the magnetic circuit. At the higher flux levels, partial saturation does indeed occur, giving rise to a flat topped flux wave containing as much as 15% harmonics.

d. The actual stator winding is concentrated in slots, and the resulting air gap flux is not sinusoidal. This causes high frequency losses, as discussed in Section 4.4.

e. In general, ferromagnetic materials are fairly good conductors of electricity. The flux distribution thus induces circulating currents in both the stator and the rotor. While this effect may be minimized by lamination, it cannot be entirely eliminated.

These, then, are the major imperfections which must be taken into account when evaluating results obtained with the infinite cylindrical model.

Mathematically, the model imposes the following boundary conditions on Maxwell's equations[6,7]:

From energy considerations, the flux density at infinity must be zero:

$$\overline{H} = \overline{B} = 0 \quad \text{at} \quad r = \infty \qquad (2.2a)$$

and at the center if must be finite

$$\overline{H}, \overline{B} \neq \infty \quad \text{at} \quad r = 0 \qquad (2.2b)$$

From cylindrical symmetry,

$$\overline{H}(r,\theta) = \overline{H}(r,\theta + 2\psi) \quad \text{and} \quad \overline{B}(r,\theta) = \overline{B}(r,\theta + 2\psi) \qquad (2.3)$$

where ψ is the pole pitch in radians, i.e., $\psi = \pi/p$

At the air gap-stator boundary,

$$H_\theta(\text{stator}) - H_\theta(\text{air gap}) = J_z \qquad (2.4)$$

At the air gap rotor boundary, H_θ is continuous:

$$H_\theta(\text{rotor}) = H_\theta(\text{air gap}) \qquad (2.5)$$

One supplementary assumption simplifies the algebra greatly: if the air gap is short, the radial component of the air gap flux does not change considerably from stator to rotor, i.e.,

At air gap boundaries $B_r(\text{stator}) = B_r(\text{rotor})$ (2.6)

These boundary conditions permit the evaluation of the arbitrary constants appearing in the solutions of Maxwell's equations in the various regions of the model.

2.4 The Solution of Maxwell's Equations.

Maxwell's equations state that in a current and charge free region curl H = div B = 0.

Expressing the z-components of the curl and the divergence in cylindrical coordinates:

$$\frac{1}{r}\frac{\delta}{\delta r}(rH_\theta) - \frac{1}{r}\frac{\delta H_r}{\delta \theta} = 0 \quad \text{and} \quad \frac{1}{r}\frac{\delta}{\delta r}(rB_r) + \frac{1}{r}\frac{\delta B_\theta}{\delta \theta} = 0$$

Since the current flow is wholly in the z-direction, $\bar{H}$ and $\bar{B}$ can have no z-components.

Thus, simplifying and letting $\bar{H} = \bar{B}/\bar{\mu}$:

$$B_\theta + r\frac{\delta B_\theta}{\delta r} - \frac{\delta B_r}{\delta \theta} = 0 \quad \text{and} \quad B_r + r\frac{\delta B_r}{\delta r} + \frac{\delta B_\theta}{\delta \theta} = 0 \qquad (2.7a, 2.7b)$$

Differentiating 2.7a with respect to r:

$$2\frac{\delta B_\theta}{\delta r} + r\frac{\delta^2 B_\theta}{\delta r^2} - \frac{\delta^2 B_r}{\delta r \delta \theta} = 0 \qquad (2.8a)$$

and differentiating 2.7b with respect to θ

$$\frac{\delta B_r}{\delta \theta} + r\frac{\delta^2 B_r}{\delta r \delta \theta} + \frac{\delta^2 B_\theta}{\delta \theta^2} = 0 \qquad (2.8b)$$

again, differentiating 2.7a with respect to θ

$$\frac{\delta B_\theta}{\delta \theta} + r\frac{\delta^2 B_\theta}{\delta r \delta \theta} - \frac{\delta^2 B_r}{\delta \theta^2} = 0 \qquad (2.8c)$$

and differentiating 2.7b with respect to r

$$2\frac{\delta B_r}{\delta r} + r\frac{\delta^2 B_r}{\delta r^2} + \frac{\delta^2 B_\theta}{\delta r \delta \theta} = 0 \qquad (2.8d)$$

multiplying 2.8a by r and adding 2.8b

$$2r \frac{\delta B_\theta}{\delta r} + r^2 \frac{\delta^2 B_\theta}{\delta r^2} + \frac{\delta B_r}{\delta \theta} + \frac{\delta^2 B_\theta}{\delta \theta^2} = 0 \tag{2.9a}$$

multiplying 2.8d by r and subtracting 2.8c

$$2r \frac{\delta B_r}{\delta r} + r^2 \frac{\delta^2 B_r}{\delta r^2} - \frac{\delta B_\theta}{\delta \theta} + \frac{\delta^2 B_r}{\delta \theta^2} = 0 \tag{2.9b}$$

Substituting 2.7a in 2.9a, and 2.7b in 2.9b

$$2r \frac{\delta B_\theta}{\delta r} + r^2 \frac{\delta^2 B_\theta}{\delta r^2} + r \frac{\delta B_\theta}{\delta r} + B_\theta + \frac{\delta^2 B_\theta}{\delta \theta^2} \tag{2.10a}$$

$$2r \frac{\delta B_r}{\delta r} + r^2 \frac{\delta^2 B_r}{\delta r^2} + r \frac{\delta B_r}{\delta r} + B_r + \frac{\delta^2 B_r}{\delta \theta^2} = 0 \tag{2.10b}$$

simplifying the last two equations yields

$$r^2 \frac{\delta^2 B_\theta}{\delta r^2} + \frac{\delta^2 B_\theta}{\delta \theta^2} + 3r \frac{\delta B_\theta}{\delta r} + B_\theta = 0 \tag{2.11a}$$

and $$r^2 \frac{\delta^2 B_r}{\delta r^2} + \frac{\delta^2 B_r}{\delta \theta^2} + 3r \frac{\delta B_r}{\delta r} + B_r = 0 \tag{2.11b}$$

It is seen that B_r and B_θ satisfy equations of the same type; the solutions must also be similar.

Solving first for B_r, a function of the coordinates and time, assume that B_r may be expressed as a product of separate functions of θ, r and t.

$$\therefore \text{ Let } B_r = \theta_r(\theta) \cdot R_r(r) \cdot T_r(t) \tag{2.12}$$

Substituting 2.12 into 2.11b, and dividing by $T_r(t)$

$$r^2 \theta_r R''_r + R_r \theta''_r + 3r \theta_r R'_r + R_r \theta_r = 0 \tag{2.13}$$

where the primes denote differentiation with respect to the independent variable.

Dividing 2.13 by $R_r \theta_r$

$$\frac{r^2}{R_r} R''_r + \frac{3r}{R_r} R'_r + 1 = -\frac{\theta''_r}{\theta_r}$$

The LHS is a function only of r, and the RHS only of θ, therefore both expressions must be equal to a constant, K_1^2 .

The θ-equation is $\Theta_r'' + K_1^2\,\Theta_r = 0$.

The solution to this is $\Theta_r = \sin(K_1\,\theta - K_2)$ (2.14)

where $K_1 = \frac{\pi}{\psi} = p$ by 2.3 and the amplitude may be set equal to unity without loss of generality.

The r-equation is

$$\frac{r^2}{R_r} R_r'' + \frac{3r}{R_r} R_r' + 1 - K_1^2 = 0 \qquad (2.15)$$

This is a form of Euler's equation,[8] and the substitution $r = e^s$ will transform it into the linear homogenous second degree equation:

$$\frac{d^2R_r}{ds^2} + 2\frac{dR_r}{ds} + (1 - p^2)R_r = 0$$

whose solution is

$$R_r = A_1 e^{(-1+p)s} + A_2 e^{(-1-p)s} \qquad (2.16)$$

Substituting $s = \ln r$ into 2.15, the radial part of the solution of 2.15 is seen to be

$$R_r = A_1 r^{(-1+p)} + A_2 r^{(-1-p)}$$

The time dependent part of the solution must be sinusoidal in view of the excitation, and involves only one arbitrary constant since the amplitude is expressed in terms of A_1 and A_2.

Thus $T_r = \sin(\omega t - K_3)$

The complete solution of 2.11b is

$$B_r = \left[A_1 r^{(-1+p)} + A_2 r^{(-1-p)}\right] \sin(p\theta - K_2)\,\sin(\omega t - K_3)$$

which may also be written as

$$B_r(r,\theta,t) = C_r r^{p-1} \sin(p\theta - \omega t + \alpha_r) + \frac{D_r}{r^{p+1}} \sin(p\theta - \omega t + \beta_r) \qquad (2.17a)$$

Similarly,

$$B_\theta = C_\theta r^{p-1} \sin(p\theta - \omega t - \alpha_\theta) + \frac{D_\theta}{r^{p+1}} \sin(p\theta - \omega t + \beta_\theta) \qquad (2.17b)$$

These equations contain eight constants, though it will be seen that not all of them are independent. The arbitrary constants will now be evaluated in terms of the boundary conditions 2.2 to 2.6.

<u>In the stator:</u>

C_r and C_θ must be zero by 2.2a. If β_r now is arbitrarily set equal to zero, and D_r equal to B_m, then all the other quantities may be evaluated in terms of B_m. Equation 2.17a shows that B_m is the maximum value of the normal component of the flux density at the stator-air gap interface ($r = R_s$). Thus,

$$B_r = B_m\left(\frac{R_s}{r}\right)^{p+1} \sin(p\theta - \omega t) \qquad (2.18a)$$

and, by the phasor relationship $B_r = \mu_s H_r e^{-j\gamma_s}$,

$$H_r = \frac{B_m}{\mu_s}\left(\frac{R_s}{r}\right)^{p+1} \sin\left(p\theta - \omega t - \gamma_s\right) \qquad (2.18b)$$

From equation 2.7: $\frac{\delta B}{\delta \theta} = pB_m\left(\frac{R_s}{r}\right)^{p+1} \sin(p\theta - \omega t)$

$$\text{i.e.,} \quad B_\theta = -B_m\left(\frac{R_s}{r}\right)^{p+1} \cos(p\theta - \omega t) \qquad (2.19a)$$

and

$$H_\theta = -\frac{B_m}{\mu_s}\left(\frac{R_s}{r}\right)^{p+1} \cos(p\theta - \omega t - \gamma_s) \qquad (2.19b)$$

<u>In the rotor:</u>

According to 2.2b, D_r and D_θ must be zero. Because of the continuity of the normal component of flux (2.6)

$$B_r = B_m\left(\frac{r}{R_r}\right)^{p-1} \sin(p\theta - \omega t) \qquad (2.20a)$$

B_θ, H_r and H_θ are evaluated exactly as before:

$$H_r = \frac{B_m}{\mu_r} \left(\frac{r}{R_r}\right)^{p-1} \sin\,(p\theta - \omega t - \gamma_r) \qquad (2.20b)$$

$$B_\theta = B_m \left(\frac{r}{R_r}\right)^{p-1} \cos\,(p\theta - \omega t) \qquad (2.20c)$$

$$H_\theta = \frac{B_m}{\mu_r} \left(\frac{r}{R_r}\right)^{p-1} \cos\,(p\theta - \omega t - \gamma_r) \qquad (2.20d)$$

<u>In the air gap</u>:

Here the flux distribution is more complicated, and varies with both positive and negative powers of r.

Thus

$$B_r = A_1 r^{p-1} \sin\,(p\theta - \omega t + \alpha) + A_2 r^{-1-p} \sin\,(p\theta - \omega t + \gamma) \qquad (2.21a)$$

and $$H_r = \frac{A_1 r^{p-1}}{\mu_o} \sin\,(p\theta - \quad + \alpha) + \frac{A_2 r^{-1-p}}{\mu_o} \sin\,(p\theta - \omega t + \gamma) \qquad (2.21b)$$

by Equation 2.7

$$H_\theta = \frac{A_1}{\mu_o} r^{p-1} \cos\,(p\theta - \omega t + \alpha) - \frac{A_2}{\mu_o} r^{-1-p} \cos\,(p\theta - \omega t + \gamma) \qquad (2.21c)$$

and $$B_\theta = A_1 r^{p-1} \cos\,(p\theta - \omega t + \alpha) - \frac{A_2 r^{-1-p}}{\mu_o} \cos\,(p\theta - \omega t + \gamma) \qquad (2.21d)$$

Equating radial flux densities at the stator boundary (2.6) at $p\theta - \omega t = 0$, and $p\theta - \omega t = \pi/2$ yields:

$$A_1 R_s^{p-1} \sin \alpha + A_2 R_s^{-p-1} \sin \gamma = 0 \qquad (2.22a)$$

and $$A_2 R_s^{p-1} \cos \alpha + A_2 R_s^{-p-1} \cos \gamma = B_m \qquad (2.22b)$$

Equating tangential m.m.f. at the rotor boundary:

$$\frac{A_1}{\mu_o} R_r^{p-1} \cos \alpha - \frac{A_2}{\mu_o} R^{-p-1} \cos \gamma = \frac{B_m}{\mu_r} \cos \gamma_r \qquad (2.23a)$$

and $$\frac{A_1}{\mu_o} R_r^{p-1} \sin \alpha - \frac{A_2}{\mu_o} R^{-p-1} \sin \gamma = \frac{-B_m}{\mu_r} \sin \gamma_r \qquad (2.23b)$$

Let $A_1' = A_1 R^{p-1}$, and $A_2' = A_2 R^{-p-1}$

Then from equations 2.22 and 2.23

$$A_1' \sin\alpha = -\frac{1}{2}\frac{\mu_o}{\mu_r} B_m \sin\gamma_r \tag{2.24a}$$

$$A_2' \sin\gamma = \frac{1}{2}\frac{\mu_o}{\mu_r} B_m \sin\gamma_r \tag{2.24b}$$

$$A_1' \cos\alpha = \frac{1}{2} B_m \left(1 + \frac{\mu_o}{\mu_r}\cos\gamma_r\right) \tag{2.24c}$$

$$A_2' \cos\gamma = \frac{1}{2} B_m \left(1 - \frac{\mu_o}{\mu_r}\cos\gamma_r\right) \tag{2.24d}$$

$$\text{Hence } \tan\alpha = -\frac{\frac{\mu_o}{\mu_r}\sin\gamma_r}{1 + \frac{\mu_o}{\mu_r}\cos\gamma_r} \doteq -\frac{\mu_o}{\mu_r}\sin\gamma_r \tag{2.25a}$$

$$\text{and } \tan\gamma = \frac{\frac{\mu_o}{\mu_r}\sin\gamma_r}{1 - \frac{\mu_o}{\mu_r}\cos\gamma_r} \doteq \frac{\mu_o}{\mu_r}\cos\gamma_r = -\tan\alpha \tag{2.25b}$$

$$A_1' = \left[\left(\frac{B_m}{2}\right)^2 \left\{1 + \frac{2\mu_o}{\mu_r}\cos\gamma_r + \left(\frac{\mu_o}{\mu_r}\right)^2\right\}\right]^{1/2} \doteq \frac{B_m}{2} \tag{2.26a}$$

$$A_2' = \left[\left(\frac{B_m}{2}\right)^2 \left\{1 - \frac{2\mu_o}{\mu_r}\cos\gamma_r + \left(\frac{\mu_o}{\mu_r}\right)^2\right\}\right]^{1/2} \doteq \frac{B_m}{2} \tag{2.26b}$$

where the approximations hold only if $\frac{\mu_o}{\mu_r} << 1$

The substitution of these constants into Equations 2.21 will yield the flux and m.m.f. distribution in the air gap.

The flux distribution in all three regions of the model has now been obtained (2.19, 2.20, 2.21) in terms of B_m; the next step is to relate B_m in magnitude and in phase to $\overline{J}$. This relation is obtained from boundary condition 2.4, which states that the discontinuity in the tangential component of m.m.f. at the stator air gap boundary is equal to the surface current density.

The tangential component of the m.m.f. in the air gap is:

$$H_\theta = \frac{B}{2\mu_o}\left\{\left(\frac{r}{R}\right)^{p-1}\cos(p\theta - \omega t + \alpha) - \left(\frac{r}{R}\right)^{-p-1}\cos(p\theta - \omega t - \alpha)\right\}$$

$$\text{where } \alpha = \tan^{-1}\left(-\frac{\mu_o}{\mu_r}\sin\gamma_r\right)$$

At the stator boundary, $r = R + \delta$, and expanding the power terms yields as a first approximation:

$$H_\theta^{(gap)} = \frac{B}{2\mu_o}\left\{\left[1 + (p-1)\frac{\delta}{R}\right]\cos(p\theta - \omega t + \alpha)\right.$$

$$\left. - \left[1 - (p+1)\frac{\delta}{R}\right]\cos(p\theta - \omega t - \alpha)\right\}$$

From Equation 2.19, the tangential m.m.f. on the stator side of the boundary is:

$$H_\theta^{(stator)} = -\frac{B_m}{\mu_s}\cos(p\theta - \omega t - \gamma_s)$$

Hence, by 2.6

$$\bar{J}_z = J(t) = H_{stator} - H_{gap}$$

$$= -\frac{B_m}{\mu_s}\cos(p\theta - \omega t - \gamma_s) - \frac{B_m}{2\mu_o}\left\{2p\frac{\delta}{R}\cos(p\theta - \omega t)\cos\alpha\right.$$

$$\left. - 2\sin(p\theta - \omega t)\sin\alpha\right\}$$

Let $J(t) = J\cos(p\theta - \omega t + \phi)$

if $p\theta - \omega t = 0$

$$J\cos\phi = \frac{B_m}{\mu_s}\sin\gamma_s - \frac{B_m}{\mu_o}\,p\,\frac{\delta}{R}\cos\alpha$$

and if $p\theta - \omega t = \pi/2$

$$J\sin\phi = \frac{B_m}{\mu_s}\sin\gamma_s - \frac{B_m}{\mu_o}\sin\alpha$$

$$\therefore \tan\phi = -\frac{\dfrac{\sin\gamma_s}{\mu_s} + \dfrac{\sin\gamma_r}{\mu_r}}{\dfrac{\cos\gamma_s}{\mu_s} + \dfrac{p}{\mu_o}\dfrac{\delta}{R}} \doteq \frac{\mu_o}{\mu_r}\frac{\sin\gamma_r}{p\,\delta/R} \qquad (2.27)$$

$$\text{and } J \doteq -\frac{B_m}{\mu_o}\, p\,\delta/R \qquad \text{if } \mu_s > \mu_r > \mu_o \tag{2.28}$$

Though it will be seen in Chapter III that in the actual test machine B_m as well as $\bar{J}$ is monitored, and the torque formula may be expressed very simply in terms of B_m, a knowledge of $\bar{J}$ is useful in order to make comparisons with other theories (2.6).

2.5 Calculation of the Torque.

As shown quantitatively in Section 1.2, the tangential component of the force on an element dS of the rotor surface is $dF = H_\theta \cdot B_r \, dS$.

From the previous section:

$$H_\theta = \frac{B_m}{\mu_r}\left(\frac{r}{R_r}\right)^{p-1} \cos\,(p\theta - \omega t - \gamma_r) = \frac{B_m}{\mu_r} \cos\,(p\theta - \omega t - \gamma_r)$$

$$\text{and} \quad B_r = B_m \left(\frac{r}{R_r}\right)^{p-1} \sin\,(p\theta - \omega t\,) = B_m \sin\,(p\theta - \omega t)$$

The total tangential force per unit length of rotor is therefore

$$F = \int_S H_\theta \cdot B_r dS = \frac{B_m^{\;2}}{\mu_r}\int_0^{2p\psi=2\pi} \cos\,(p\theta - \omega t - \gamma_r)\,\sin\,(p\theta - \omega t)\,Rd\theta$$

$$= \frac{B_m^{\;2}\pi R}{\mu_r}\,\sin\,\gamma_r$$

$$\text{and the torque is } T = R\cdot F = \frac{\pi R^2 B_m^{\;2} \sin \gamma_r}{\mu_r} = VB_m^{\;2}\,\frac{\sin\gamma_r}{\mu_r} \tag{2.29}$$

where V denotes the volume of the rotor.

$$\text{By 2.1} \quad \frac{\pi B_m^{\;2}}{\mu_r}\,\sin\gamma_r = \pi B_1 H_1 \,\sin\alpha = A$$

$$\text{Therefore} \qquad T = \frac{VA}{\pi} \tag{2.30}$$

where A is the area of the hysteresis ellipse traced out by the peripheral value of the radial flux density.

It is rather interesting to note by comparing 2.30 to Steinmetz's and Roters' formula, or by direct integration, that the total energy loss is

$$\int_V \left[\oint H_r (r_1\theta) d B_r (r_1\theta)\right] d V + \int_V \left[\oint H_\theta \, d B_\theta\right] dV = \frac{2}{p} AV$$

This explains the similarity in the appearance of the two formulae as well as the origin of the factor of p/2.

In Chapter IV the torque calculated from Equation 2.30 will be compared to the measured values, and discrepancies discussed.

2.6 <u>The Energy Transfer Method</u>.

The algebra in the previous section may be partially verified by calculating the energy transfered from the stator to the rotor at synchronous speed.

In the model of Section 2.3, the flow of current at the stator surface is opposed only by the counter-e.m.f. induced by the rotor. The magnitude of this counter-e.m.f., E_z, may be calculated from Maxwell's equations:

$$\text{curl } \overline{E} = -\frac{\delta B}{\delta t} \tag{2.31}$$

Taking the radial component of both sides of Vector Equation 2.31,

$$\text{curl}_r \overline{E} = \frac{1}{r}\frac{\delta E_z}{\delta \theta} - \frac{\delta E_\theta}{\delta z} = -\frac{\delta B_r}{\delta t}$$

since $\dfrac{\delta E_\theta}{\delta z} = 0$

Equation 2.19 shows that at the stator boundary

$$\frac{1}{R_s}\frac{\delta E_z}{\delta \theta} = -\omega B_m \cos (p\theta - \omega t)$$

$$\text{or} \quad E_z = -\frac{\omega}{p} R B_m \sin (p\theta - \omega t) \tag{2.32}$$

The energy flow through a cross-sectional area is $E = \int_A \overline{J} \cdot \overline{E} \, dA$

or, using 2.32, 2.27 and 2.28,

$$= \int \left\{ - \frac{B_m}{\mu_o} p \frac{\delta}{R} \cos \left(p\theta - \omega t - \frac{\sin \gamma_r}{\mu_r \left(\frac{p}{\mu_o} \frac{\delta}{R} \right)} \right) \right\} \cdot$$

$$\left\{ - \frac{\omega}{p} R\, B_m \sin (p\theta - \omega t) \right\} \; R d\theta$$

$$= \frac{B_m^{\;2}}{\mu_o} R^2 \pi\, p \frac{\delta}{R} \sin \frac{\sin \gamma_r}{\mu_r \left(\frac{p}{\mu_o} \frac{\delta}{R} \right)}$$

$$= \frac{\omega}{p} \frac{B_m^{\;2}}{p \mu_r} \pi R^2 \sin \gamma_r \quad \text{since} \left[\frac{\sin \gamma_r}{\mu_r \left(\frac{p}{\mu_o} \frac{\delta}{R} \right)} \right] \ll 1$$

Now Torque $= \dfrac{\text{Energy}}{\text{angular velocity}}$, and the angular velocity $\dfrac{d\theta}{dt} = \dfrac{\omega}{p}$

$$T = \frac{1}{\mu_r} B_m^{\;2} V \sin \gamma_r \text{ , as in Equation 2.29.}$$

2.7 The Flux-Pattern in the Hysteresis Motor.

In order to gain a better understanding of the secondary phenomena in the hysteresis motor, it may be worthwhile to study the flux distribution in the stator and the rotor in greater detail than would be possible directly from Equations 2.19 and 2.20. In this section the coordinate equations of the actual flux-lines will be developed, and the patterns plotted for the 2-pole and the 4-pole cases.

In the rotor:

From Equation 2.20,

$$B_r = B_m \left(\frac{r}{R_r} \right)^{p-1} \sin (p\theta - \omega t)$$

$$B_\theta = B_m \left(\frac{r}{R_r} \right)^{p-1} \cos (p\theta - \omega t)$$

For the sake of simplicity, the flux line will be plotted at t = 0.

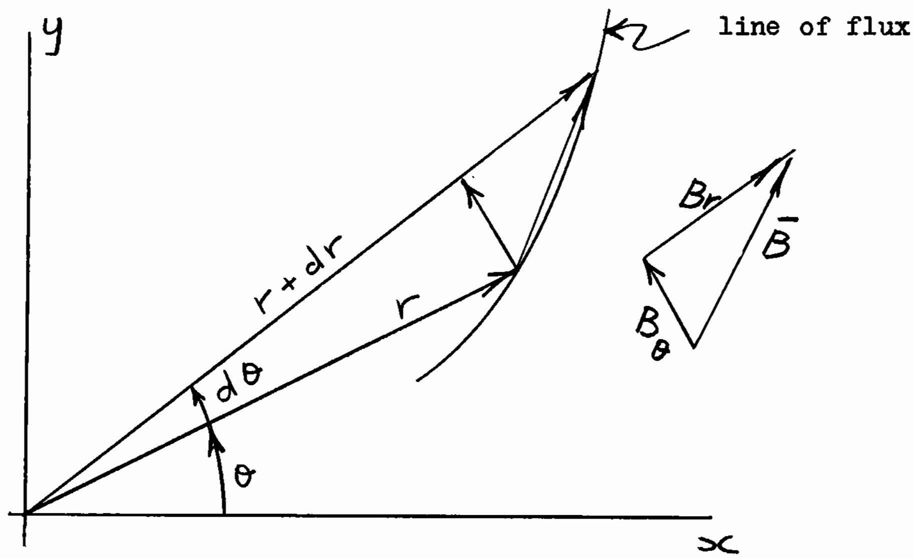

Fig. 2.3 Diagram for Deriving Coordinate Equations of Lines of Force

Then from Fig. 2.3

$$\frac{r d\theta}{dr} = \frac{dB_\theta}{dB_r} = -\tan p\theta$$

$$\therefore \ln r = \int -\frac{d\theta}{\tan p\theta} = -\frac{1}{p}\ln \sin p\theta - \ln C$$

$$\therefore Cr^{-p} = \sin p\theta$$

Thus, for p = 1, $\frac{C}{r} = \sin \theta$

or, in rectangular coordinates, y = C.

These are horizontal straight lines.

For p = 2, $Cr^{-2} = \sin 2\theta = 2 \sin \theta \cos \theta$

or $C = 2xy$

These are rectangular hyperbolae asymptotic to the x and y axes.

Similarly, for $p > 2$, higher order hyperbolae result, asymptotic to rays at $2\pi/2p$ radians.

<u>In the stator:</u>

From Equation 2.19

$$B_r = B_m \left(\frac{R_s}{r}\right)^{p+1} \sin(p\theta - \omega t)$$

$$B_\theta = -B_m \left(\frac{R_s}{r}\right)^{p+1} \cos(p\theta - \omega t)$$

and $\dfrac{rd\theta}{dr} = \tan p\theta$ at $t = 0$

Integrating this equation results in

$$Cr^p = \sin p\theta$$

Thus for $p = 1$, $Cr = \sin\theta$

or $$C\sqrt{x^2 + y^2} = \frac{y}{\sqrt{x^2 + y^2}}$$

$$\therefore \quad x^2 + \left(y - \frac{1}{2C}\right)^2 = \frac{1}{4C^2}$$

This equation represents circles of radius $\frac{1}{2C}$, with centres at $(0, \pm \frac{1}{2C})$

For $p = 2$, $Cr^2 = \sin 2\theta$ (2.33a)

in rectangular coordinates: $C(x^2 + y^2) = 2xy$ (2.33b)

Now let $\omega = u + i\,v = \dfrac{1}{z} = \dfrac{1}{x + i\,y} = \dfrac{x}{x^2 + y^2} - \dfrac{iy}{x^2 + y^2}$

by 2.33b

$$\therefore \quad \omega = \pm \frac{x}{\sqrt{\frac{2}{C}}\sqrt{xy}} - \pm \frac{iy}{\sqrt{\frac{2}{C}}\sqrt{xy}} = K\sqrt{\frac{x}{y}} \pm i\,K\sqrt{\frac{y}{x}}$$

$$\therefore \quad u = K\sqrt{\frac{x}{y}}, \qquad v = -K\sqrt{\frac{y}{x}}$$

$$\therefore \quad uv = \pm K^2 = \pm C/2$$

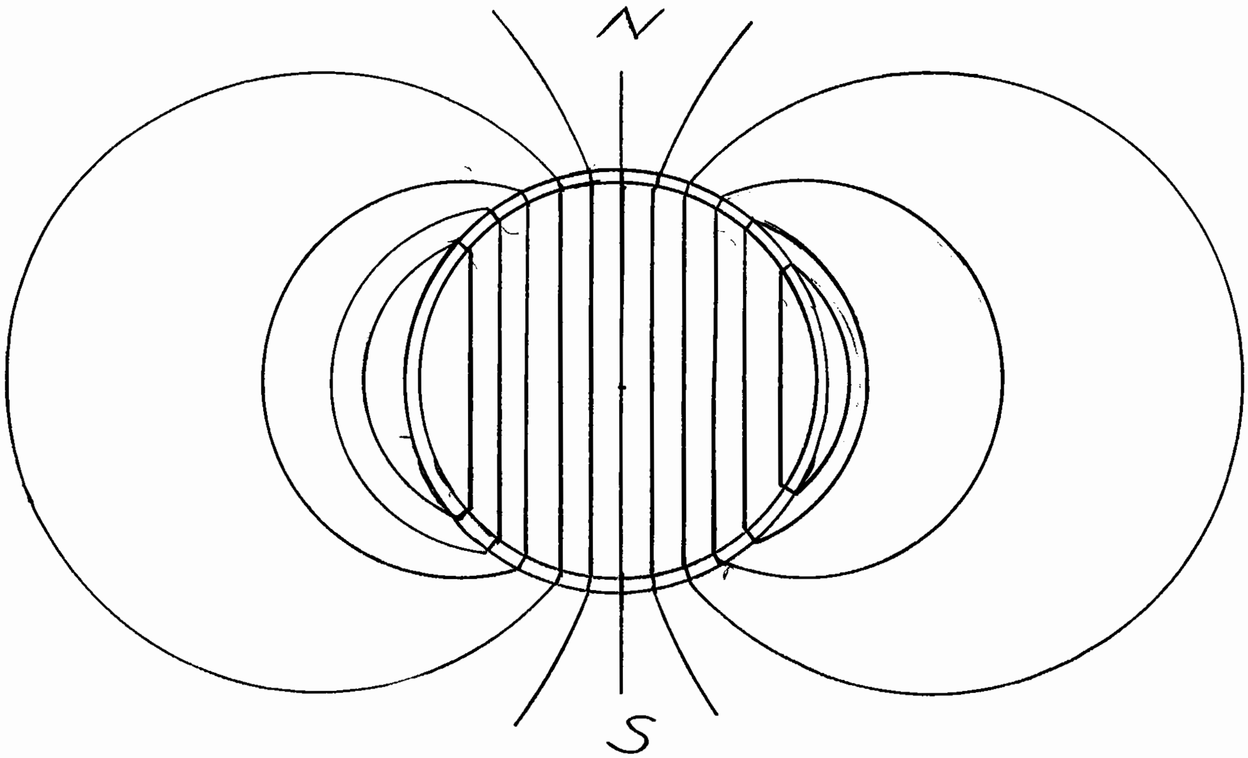

Fig. 2.4a Flux Distribution in 2-pole Machine.

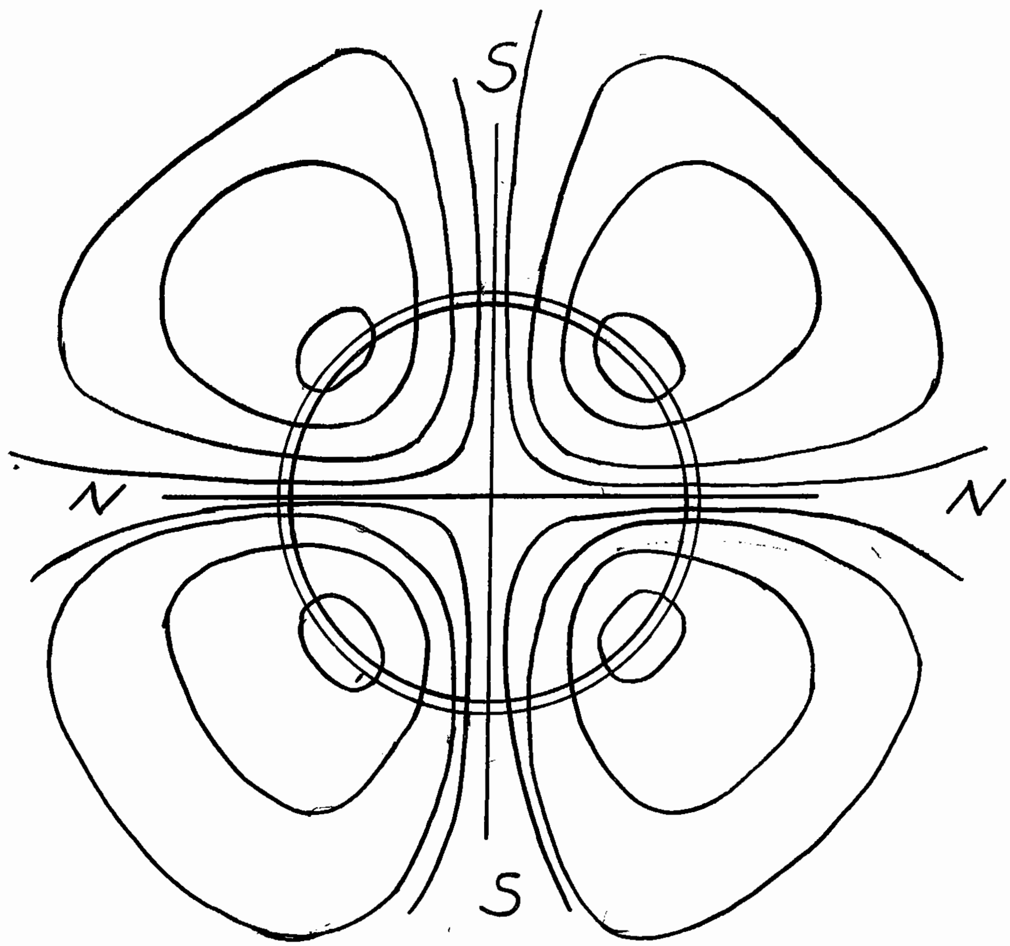

Fig. 2.4b Flux Distribution in 4-pole Machine.

i.e., 2.33a represents the inverse of a rectangular hyperbola with respect to a circle with center (0,0) and radius $\sqrt{\frac{2}{c}}$.

The flux lines are plotted in Fig. 2.4. Note that the lines of force (direction of m.m.f.) form a similar pattern, displaced by the angle γ_s or γ_r. It may be seen from the pattern that the finite dimensions of the stator and the presence of the rotor shaft are likely to have the greatest effect in the 2-pole case. In multi-pole construction, the thin cylinder design becomes more and more economical as the number of poles increases.

CHAPTER III

Description of the Test Machine

3.1 The Stator.

In order to examine as many as possible of the variables in the theory derived in the previous chapter, the rotor was tested with three different stators. The stators were all made up from laminations originally intended for a 3/4 H.P., 4-pole induction motor, with the following design parameters:

Ratings:		Stator Winding:	
Horsepower	3/4	Winding Type	Lap
Volts	208	Connection	Y
Phases	3	Slots/phase/pole	3
Frequency (c.p.s.)	60	Turns/coil	21
R.P.M.	1800	Conductors/phase	504
Amperes (full load)	2.6	Conductor size	No. 19
Temperature Rise	40°	Pitch coil	1-8
Efficiency	75%	Resistance/phase	2.95 ohms

One of the stators was wound as specified above, while the other two were fitted with two and six pole 208 volt short pitched windings as shown in the design data sheet in the Appendix. Fig. 3.1 shows the distribution of the phase belts in the two pole stator, and the wave shape which would result if the phase belts consisted of current sheets instead of isolated coils in slots. It will be shown in Chapter IV that local variations (slot ripple) have a far greater effect upon performance than the overall distribution factor of the winding.

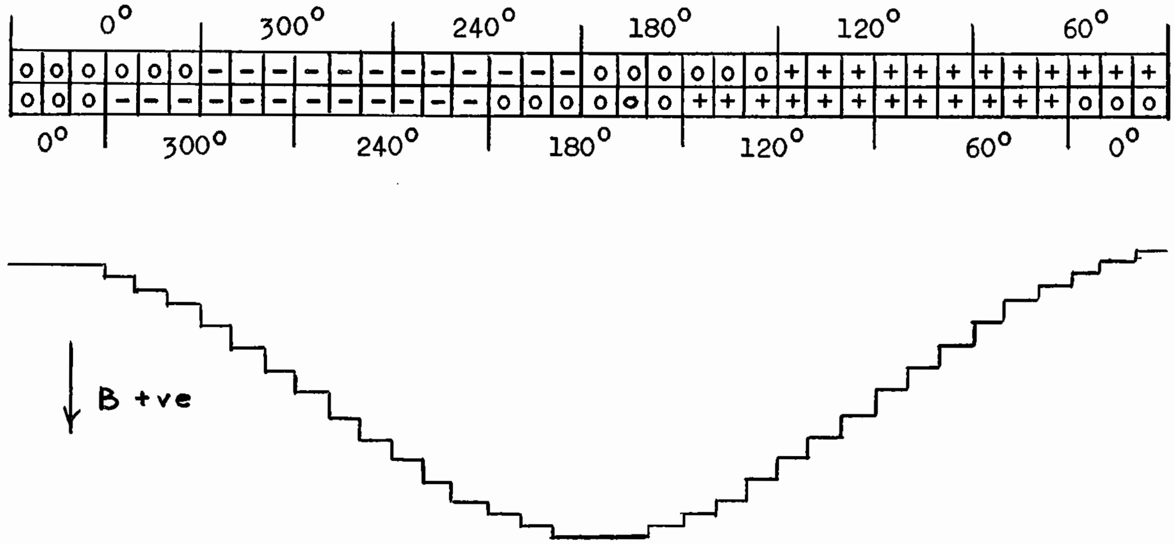

Fig. 3.1 Phase Belts in 4-p Stator Winding

To measure flux densities at the air gap, a single turn of fine wire was inserted in stator slots one pole-pitch apart. Values obtained with these probes were checked against those from similar probes around single teeth and around the yoke itself; after allowance had been made for leakage flux at the junction of the phase belts, the values agreed to within the accuracy of the measuring instruments (3%).

3.2 <u>The Rotor</u>.

The rotor (Fig. 3.2) was constructed of .014" thick Vicalloy laminations pressed together on a 1/2" shaft. The laminations were sprayed on each side with lacquer to prevent eddy currents, and 1/4" plastic end discs provide a high reluctance path for leakage fluxes.

An average air gap of .016" at least was found to be necessary because of slight irregularities and excentricities in the stator construction. The rotor laminations were punched to a slightly larger diameter, heat treated,

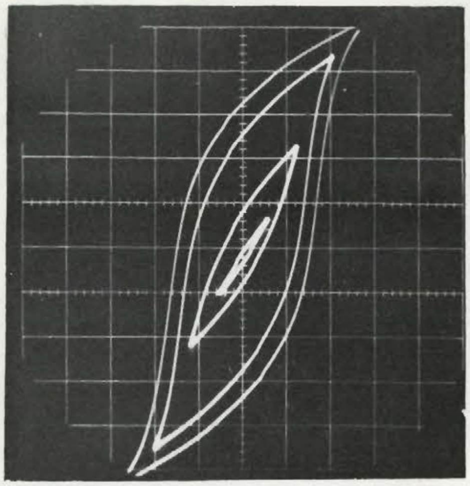

Fig. 3.7a Family of Hysteresis Loops of Vicalloy.

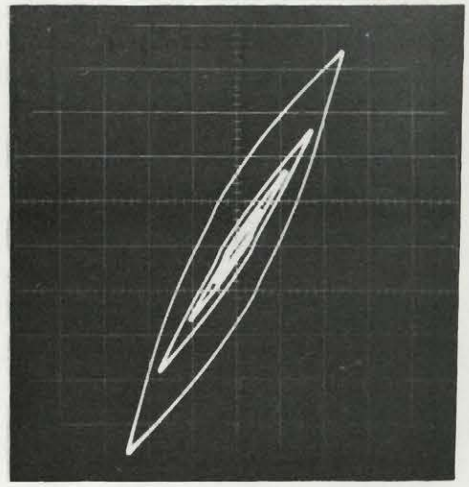

Fig. 3.7b Hysteresis Loop at Low Flux Densities.

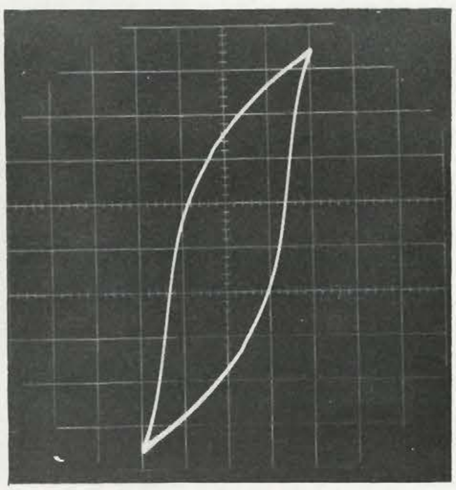

Fig. 3.7c Hysteresis Loop at Medium Flux Densities.

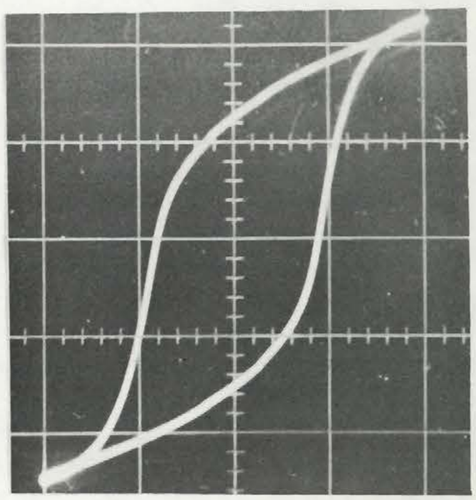

Fig. 3.7d Hysteresis Loop at High Flux Densities.

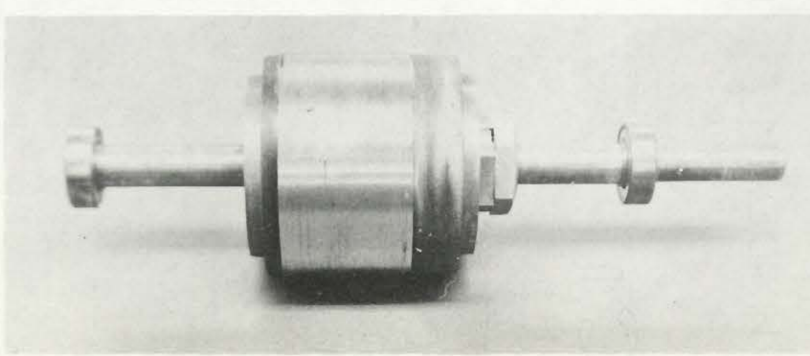

Fig. 3.2 Vicalloy Rotor

and then ground to the final dimensions.

The rotor material, Vicalloy, is a carbon free permanent magnet alloy composed of 38% iron, 10% vanadium, and 52% cobalt. It is available in strip form, and before the final heat treatment it may be machined without special equipment (though not without difficulty: Rockwell hardness 41-42)[9].

The aging heat treatment, designed to increase the size of the Vicalloy B-H loop (Section 3.4), consists of baking the alloy for a period of four hours at 1110°F. Upon completion of this process, Vicalloy attains a hardness comparable to that of tool steel (Rockwell number 62-63).

Since the manufacturers of Vicalloy state that very large variations in the magnetic properties are encountered among individual batches of this material, it was necessary to establish these properties experimentally, using the manufacturer's data merely for qualitative guidance. The experimental procedure is described in the next two Sections.

3.3 Magnetic Measurements - Direct Current Method.

While in other applications it is usually sufficient to have a very approximate idea of the size and shape of the hysteresis loop in order to establish the losses due to it, in hysteresis motor design this data is of course of paramount importance. The customary d.c. method, about to be described, was first applied in an attempt to obtain a fairly accurate picture of the B-H curve.

A toroidal sample was prepared, with dimensions as follows:

Inner diameter	.080 meter
Outer diameter	.100 meter
Thickness (seven laminations)	.0025 meter
Cross-sectional area	$.25 \times 10^{-4}$ m^2
Number of turns in magnetizing winding (No. 12 wire)	370
Number of turns in search coil (No. 23 wire)	180
Mean Radius (R_o)	.045 meter

The evenly distributed secondary winding was wound next to the magnetic material, and the four-layer magnetizing winding outside; this arrangement minimizes errors due to leakage flux. The flux distribution is assumed to be uniform throughout the cross-sectional area of the toroid. With the above dimensions the resultant error is of the order of $^{10}\frac{1}{12}\frac{(2r)^2}{(R_o-r)^2} = 0.4\%$

where r is the radius of the cross section

and R_o is the mean radius

The magnetic intensity in the sample is

$$H = \frac{NI}{L} = \frac{NI}{2\pi R_o} = \frac{370 \times I}{2\pi(.045)} = 1308\ I\ \frac{\text{Turns}}{\text{Meter}} \quad (= 16.4\ I\ \frac{\text{Oersteds}}{\text{Ampere}})$$

where I is the current (amps.) in the magnetizing winding

The flux density B was measured with a flux meter having a maximum sensitivity of 10^{-4} weber-turns/division (10,000 maxwell-turns/division). Thus

$$B = \frac{\phi}{A} = \frac{10^{-4}d}{.25\times10^{-4}\times180} = .0222\ d\ \frac{\text{weber}}{m^2}/\text{division} \quad (= 222\ d\ \text{gauss/division})$$

where B = change in flux density

ϕ = change in total flux linking toroid

A = cross-sectional area of toroid

d = deflection of flux meter in divisions (most sensitive range).

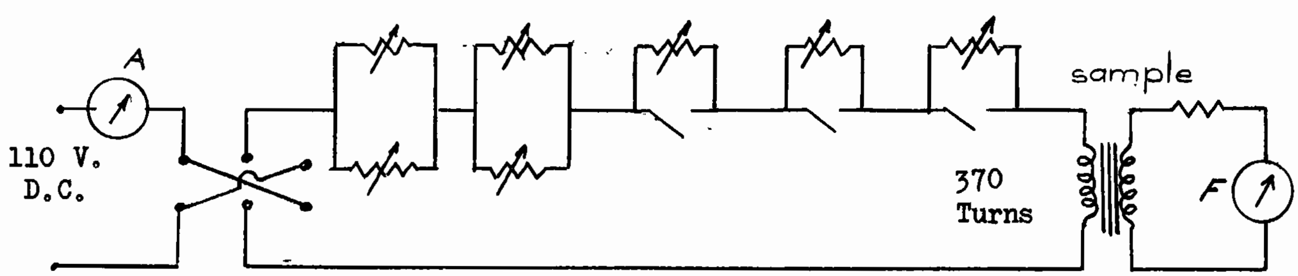

A = Ammeter
F = Fluxmeter

Fig. 3.3 Circuit Diagram for D.C. Hysteresis Measurements.

The circuit used in measuring B and H is shown in Fig. 3.3. The magnetizing current may be varied in discrete steps by switching resistors in and out, and corresponding deflections of the flux meter noted. Since the flux meter measures only changes in flux, the peak values of B are obtained by halving the maximum change.

To have the sample traverse a hysteresis loop of the desired magnitude, it is important to bring the material to cyclic condition first by reversing the peak current fifteen or twenty times. A typical set of data, and the corresponding hysteresis loop, are shown in Table I and Fig. 3.4.

- TABLE I -

Point	Current I	Deflection d	H amp/m.	B weber/m^2
		43.0		
1	22	42.0	4.53	+ .780
2	18	36.4	3.73	+ .656
3	14	32.2	2.90	+ .563
4	10	27.0	2.07	+ .457
5	0	17.5	0	+ .247
6	- 10	3.2	- 2.07	- .071
7	- 14	7.0	- 2.90	- .297
8	- 18	21.5	- 3.73	- .617
9	- 22	28.3	- 4.52	- .780
10	- 18	24.8	- 3.73	- .702
11	- 14	21.3	- 2.90	- .624
12	- 10	17.8	- 2.07	- .546
13	0	8.5	0	- .335
14	10	5.5	2.07	- .025
15	14	15.5	2.90	+ .197
16	18	32.3	3.73	+ .570

10,000 gauss = 1 weber/m^2.

126 oersteds = 1 amp/m.

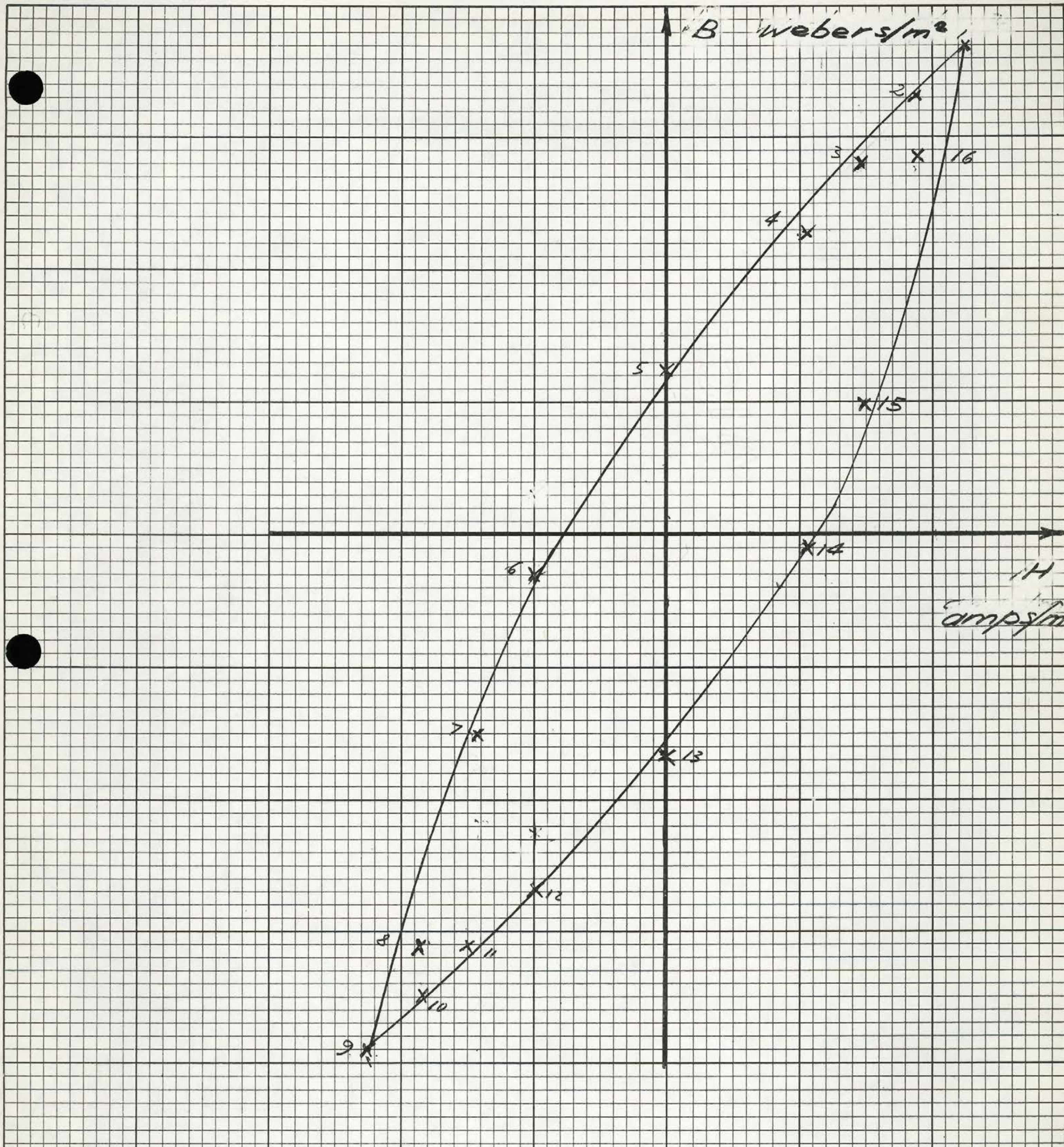

Fig. 3.4 B.H. Loop of Vicalloy-D.C. Method

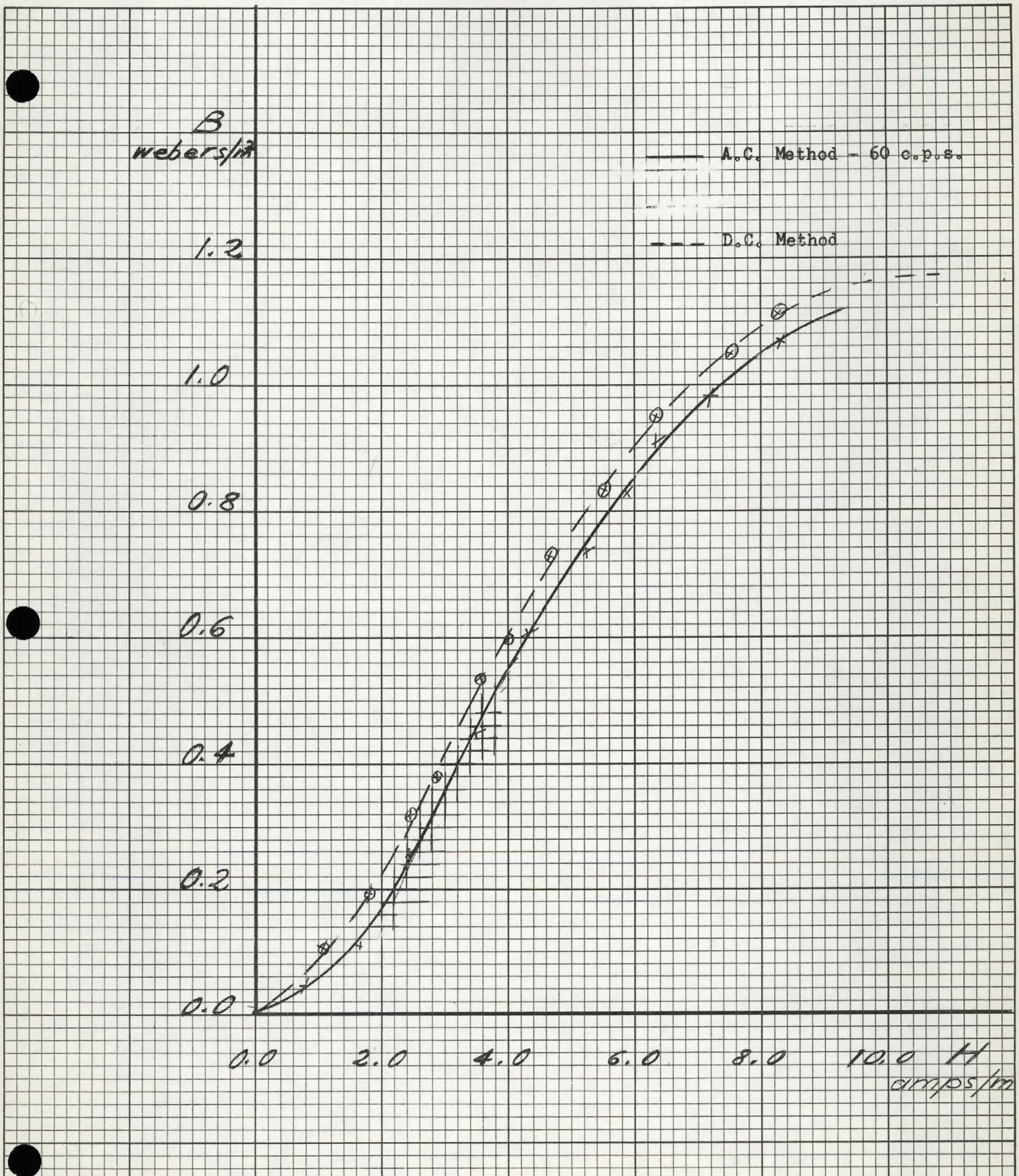

Fig. 3.5 Magnetization Curves of Vicalloy

Very large currents - of the order of 40-50 amps. - are necessary to even partially saturate the sample, and with such a small specimen heat dissipation poses a problem. High temperatures tend to damage the insulation of the coils, and also raise the resistance of the windings appreciably, making it difficult to keep the magnetizing current constant during a reading. For this reason the experimental curves have inaccuracies of the order of 15%, and the loops never close upon themselves.

The poor results achieved by the method just described made an alternative derivation of the B-H loop imperative. The next section deals with an a.c. method of obtaining the hysteresis loop.

The d.c. method may nevertheless be used as a check on the a.c. method by comparing the magnetization curves (Fig. 3.5) yielded by the two. Since less switching is required in deriving this curve, the d.c. method proves sufficiently reliable for this purpose, and it is reassuring to see that the two curves never differ by more than 5%.

3.4 Magnetic Measurements - A.C. Method.

The toroidal sample already described was used in this set of measurements. The circuit is shown on Figure 3.6.

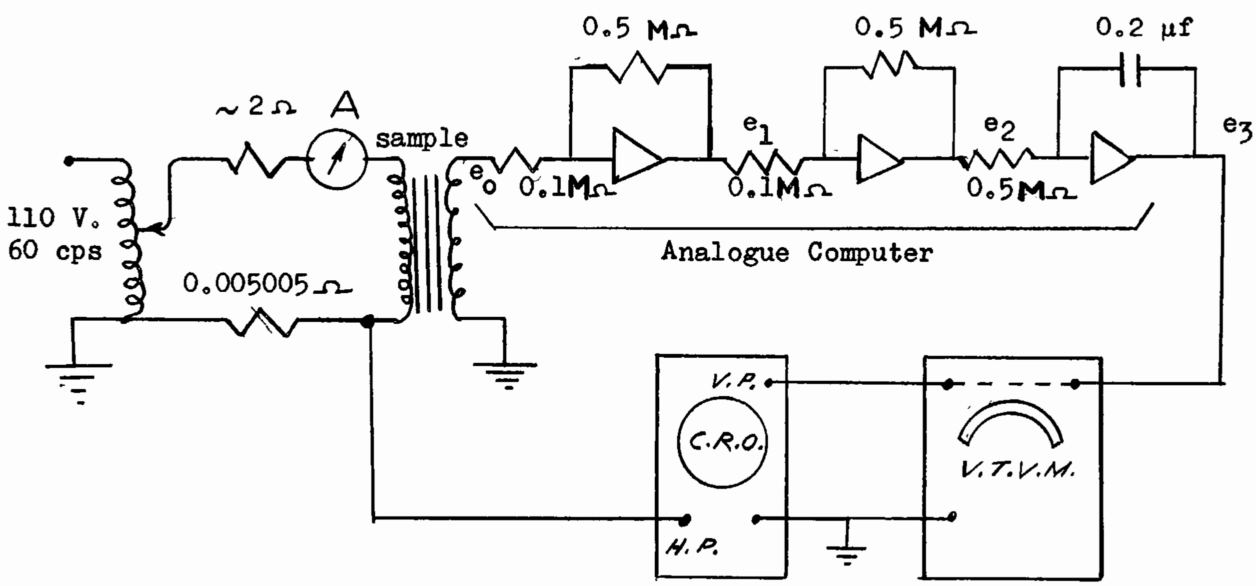

Fig. 3.6 Circuit Diagram for A.C. Method of Measuring B-H Loop.

The essence of this method consists of applying a signal instantaneously proportional to the 60 cps magnetizing current, and therefore to H, to the horizontal deflection plates of an oscilloscope, and a signal proportional to the integral of the voltage generated in the search coil, and therefore to $B = \phi/A = \frac{1}{A}\int e_2 dt$ to the vertical plates[11]. The hysteresis loop of the material then appears on the oscilloscope screen. It is true that the pattern will have a somewhat increased width because of the presence of eddy currents, but the interlamination insulation and the high resistivity of Vicalloy tend to minimize this distortion.

$$H \text{, as before, is } 1308 \; I(\text{peak}) \; \frac{\text{Turns}}{\text{Meter}} \quad \left(= 16.4 \; \frac{\text{Oersteds}}{\text{Amp(peak)}}\right) \tag{3.1}$$

and B is calculated as follows:

$$e_2 = (-)\, n_2 \frac{d\phi}{dt}$$

$$\therefore \quad \phi = (-)\, \frac{1}{n_2} \int e_2 dt$$

$$\text{and} \quad e_3 = M \int e_2 dt = -\, M\, n_2\, \phi$$

where M is the amplification factor of the system

$= 5 \times 5 \times 10 = 250$

e_3 is in volts

ϕ is in webers (10^8 maxwells)

$$\text{thus} \quad B = \frac{\phi}{A} = \frac{e_3}{Mn_2A} = .89 \; \frac{\text{webers}}{m^2}/\text{volt} \quad (= 8.9 \quad \text{gauss/millivolt}) \tag{3.2}$$

The area of the hysteresis curve may then be determined by photographing the loop on the screen and measuring the area. It is of course necessary to keep note of the scale settings in order to calibrate the axes in terms of equations 3.1 and 3.2.

The loop area may be expressed in

$$\frac{\text{webers}}{m^2} \times \frac{\text{amps}}{m} = 40\pi \text{ gauss oersteds}$$

$$1\ \frac{\text{weber amp}}{m^3} \text{ is also equivalent to } \frac{10^4}{6.1} \text{ joules/in}^3$$

(a common unit in hysteresis motor design practice)

Photographs of typical loops are shown in Fig. 3.7, while the loop area is plotted against maximum flux density on linear scale in Fig. 3.8 and on logarithmic scale on Fig. 3.9.

The amplification and integration of the signal from the secondary winding were achieved by means of a small analogue computer (Fig. 3.10). Although the output of the secondary winding was of the order of millivolts, sufficiently large to trigger an oscilloscope, this was reduced by a factor of almost 400 during integration. The amplification back to the original level had to take place in three stages because of drift in the computer amplifiers. Ten 1% resistors were used (because several values shown in the circuit diagram had to be made up of parallel combinations) and, taking into account the slight non-linearity of the amplifiers, the resulting accuracy cannot be expected to be better than 4%. An additional inaccuracy is introduced by the presence of noise (2 millivolts output), but this is almost insignificant.

The a.c. method, in spite of the sources of error indicated above, constitutes a simple and rapid means of determining the hysteresis loop of a toroidal sample, especially when the values for several peak flux densities are required.

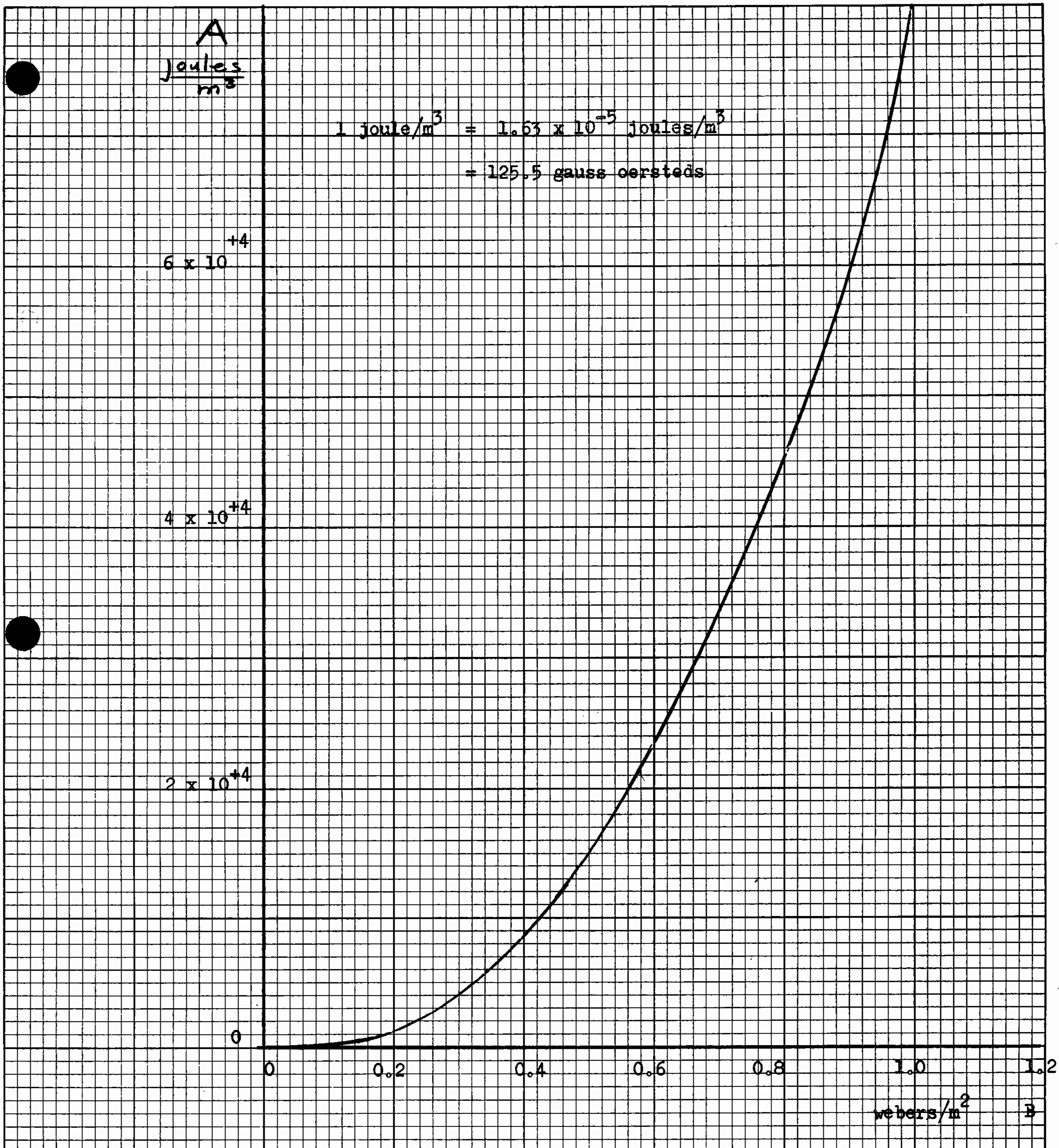

Fig. 3.8 Graph of Area of Hysteresis Curve vs. Flux Density

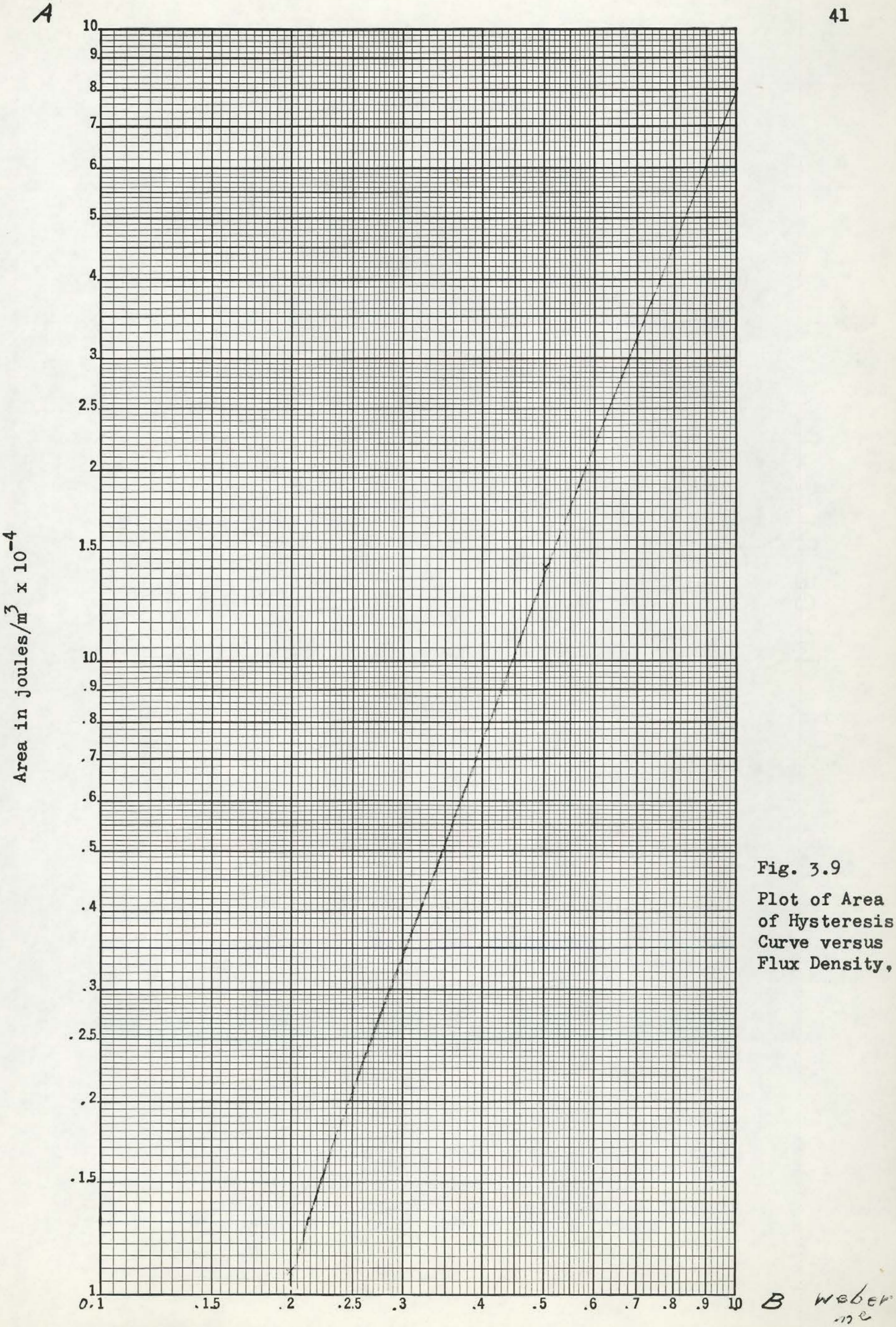

Fig. 3.9

Plot of Area of Hysteresis Curve versus Flux Density.

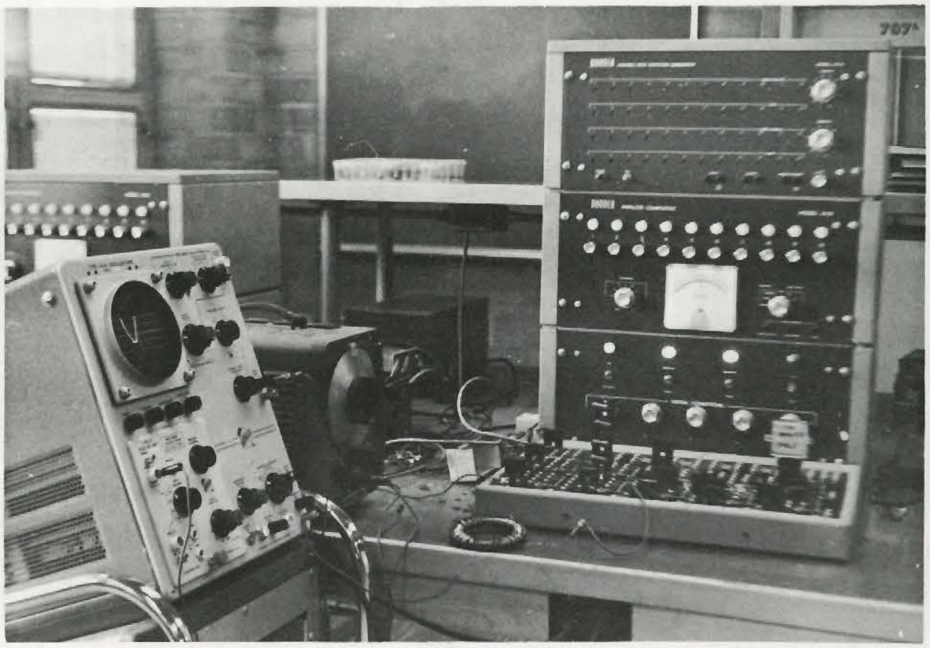

Fig. 3.10 Apparatus for Magnetic Testing-A.C. Method.

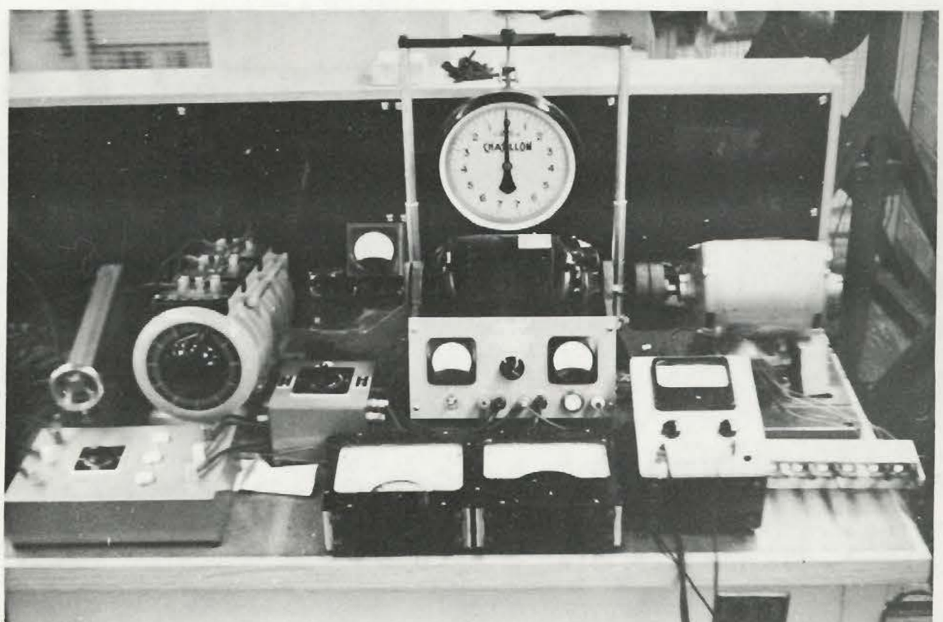

Fig. 4.2 Apparatus for Testing Torque Chacteristics of Hysteresis Motor.

CHAPTER IV

Asynchronous Performance

4.1 Methods of Measurement.

A circuit diagram of the apparatus used in measuring the various characteristics of the experimental hysteresis motor is shown in Fig. 4.1, and a photograph of the actual layout in Fig. 4.2.

The essential features comprise a metered variable frequency alternating current supply to the hysteresis motor and a 3/4 H.P. direct current dynamometer coupled to the same shaft. A 2 H.P. Ward-Leonard set constitutes a variable voltage d.c. supply for the armature of the dynamometer, while the field of this machine is connected through a rheostat to the 220 V mains. The torque is measured by a 0 to 7.5 lb. or a 0 to 1 lb. spring balance mounted 6" from the shaft of the dynamometer; the torque readings given in the rest of this chapter and the next one are the average of readings taken in the forward and reverse directions, and may be considered accurate to within .03 ft.-lbs. A permanent magnet type d.c. tachometer mounted on the dynamometer shaft gives speed to within 50 r.p.m. Close to synchronism a stroboscope permits more accurate readings.

The metering system consists of voltmeters and ammeters in the three a.c. lines to the hysteresis motor, and a wattmeter which may be switched between the lines without disrupting the current. A single wattmeter instead of the customary two was used in power measurements in an effort to increase the accuracy at the dominant low power factors. Where maximum accuracy was not deemed important a double element wattmeter replaced the switching arrangement.

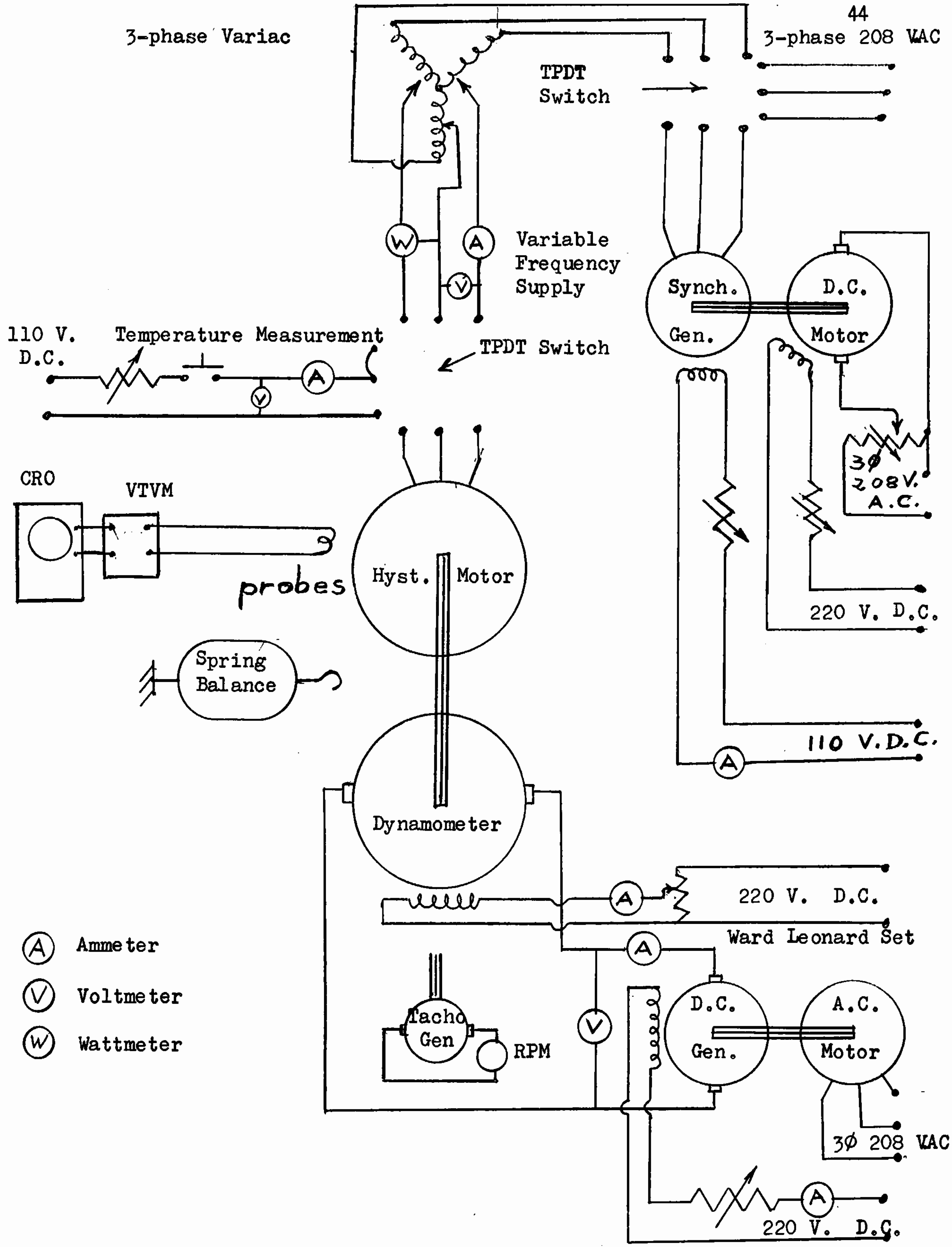

Fig. 4.1 Circuit Diagram of Measuring Apparatus.

The flux density at the air gap, i.e. the e.m.f. generated in the probes around the stator poles, was measured by means of an electronic tube voltmeter and an oscilloscope (Section 4.2). The e.m.f. and the flux density are related as follows:

$$e = -n\frac{d\phi}{dt} = \omega\,\phi_{max}\sin\omega t \qquad \text{since } n = 1$$

$$\therefore\; e_{max} = \omega\,\phi_{max}$$

$$\therefore\; B_{max} = \frac{\phi_{max}}{A} = \frac{e_{max}}{\omega A} = 2.65\,\frac{e_{max}}{A}\,\frac{\text{webers}}{m^2} \quad \left(= 265\,\frac{e_{max}(mV)}{A(cm2)}\ \text{gauss}\right)$$

where A is the effective area of the search coil in m^2.

The formula just deduced applies only if the width of the search coil is small compared to the pole-pitch. If the search coil encompasses the whole poleface, then the distribution of the flux (sinusoidal) through the poleface must also be taken into account, and the above result multiplied by a factor of $\pi/2$ in order to obtain the true maximum flux density. These measurements were checked with a Hall-effect flux density meter, which did not, however, prove reliable to within better than 10%.

Provisions are also made to monitor the temperature of the hysteresis motor by means of resistance measurements on the stator winding. The necessary voltmeter-ammeter arrangement is also shown in Fig. 4.1. With a suitable choice of meters the temperature may be read directly on the voltmeter once the current has been set to a predetermined constant value.

4.2 Torque.

It was shown in Chapter II that in the idealized hysteresis motor the torque developed does not vary with speed provided the flux density is maintained constant. Consequently, the variation of torque with speed in the real motor serves as an indication of the magnitude and nature of the secondary phenomena influencing hysteresis motor behaviour.

A simple means of obtaining directly some measure of the change in torque with speed consists of connecting the output of the tachogenerator to a graphic recorder, and suddenly reversing the polarity of two windings of the hysteresis motor. This results in the motor accelerating from minus synchronous speed to plus synchronous speed at a rate (slope) proportional to the torque. Figure 4.3 shows the results of such a test on the four pole machine. It may be seen that the slope of the envelope is practically constant between $-\omega_0$ and 0, and between 0 and $+\omega_0$, although there is considerable difference between the two. This difference is due only partly to friction, which tends to increase the slope at negative speeds and decrease it at positive speeds.

The test just described was also repeated with a photographic type recorder, which offers the advantage of a larger channel width. Here the d.c. output of the dynamometer at constant excitation was taken as the speed-dependent signal. Results are shown in Fig. 4.4. A curve of the free deceleration is also given; this shows that friction is practically constant throughout the speed range considered.

More detailed graphs of the torque speed variation with all three stators and at different flux densities are shown in Fig. 4.5. Two features are of great interest in these graphs: the gradual change in the torque at asynchronous speeds, and the sudden jump at synchronism (where the sign of the torque also changes).

Although the torque resolution of the spring balance is not sufficiently high (because of vibration and instability in the d.c. system) to compare the gradual increase in torque with slip to theoretically calculated values, it seems certain that this variation is due to the induction motor effect caused by eddy currents. As already mentioned in Chapter I, the presence of laminations reduces this effect very considerably.

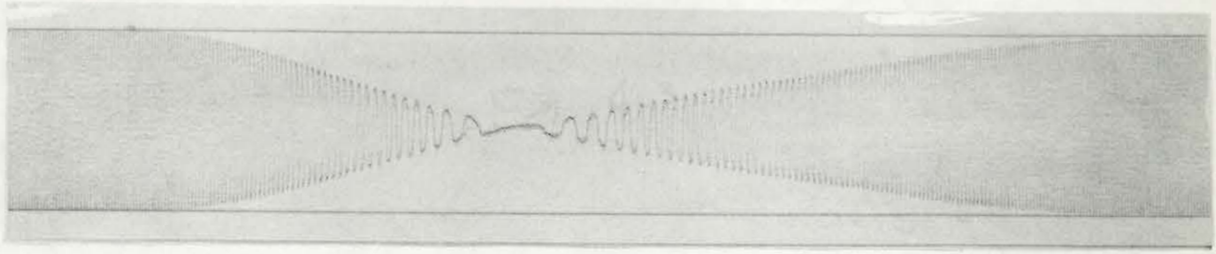

Fig. 4.3 Deceleration and Acceleration - 2-pole stator - at Phase-to-Phase Terminal Voltage = 150 V.-A.C. Tachometer.

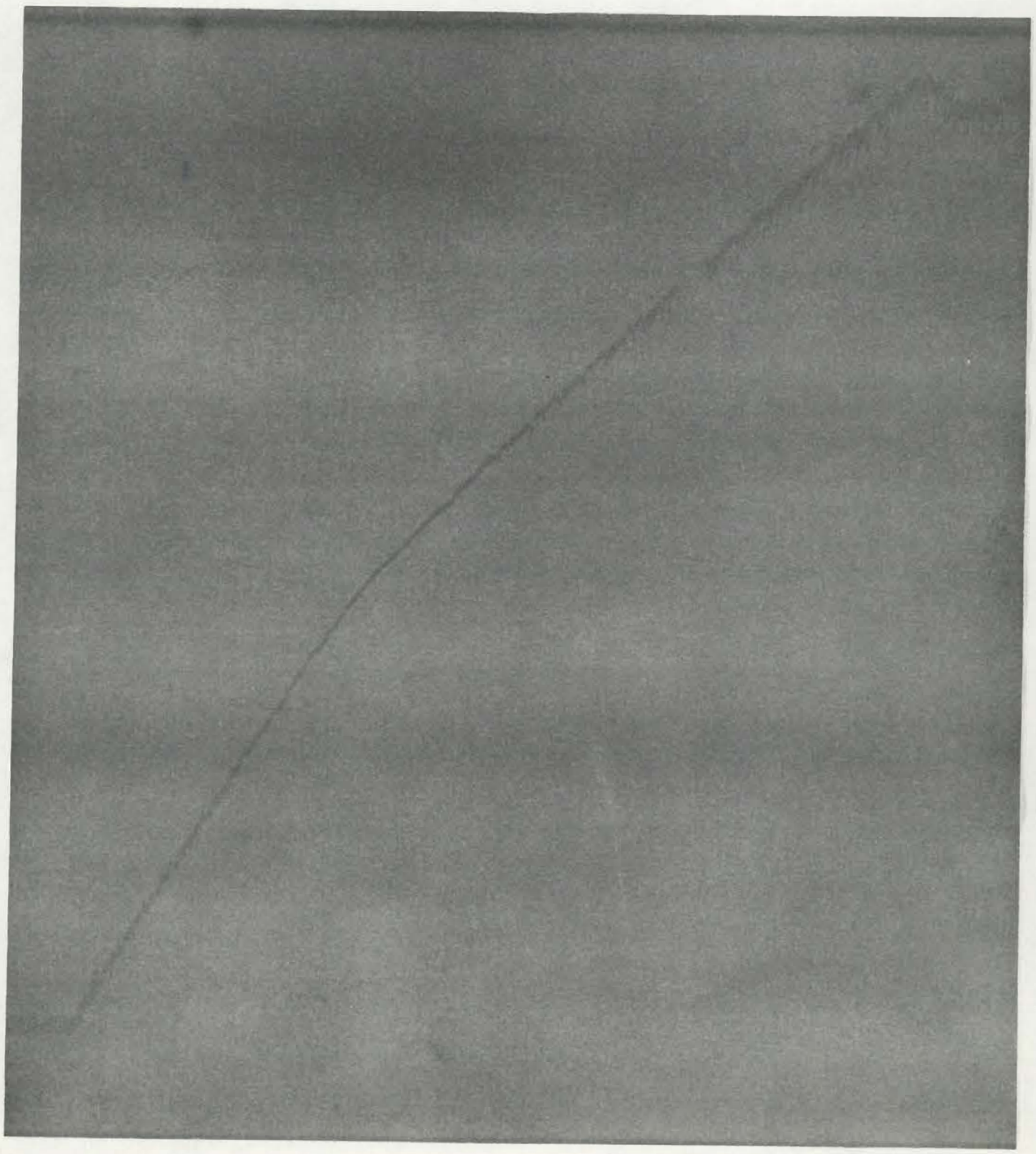

Fig. 4.4a Deceleration and Acceleration - 2-pole stator - at Phase-to-Phase Terminal Voltage = 160 V.-D.C. Tachometer and Visicorder.

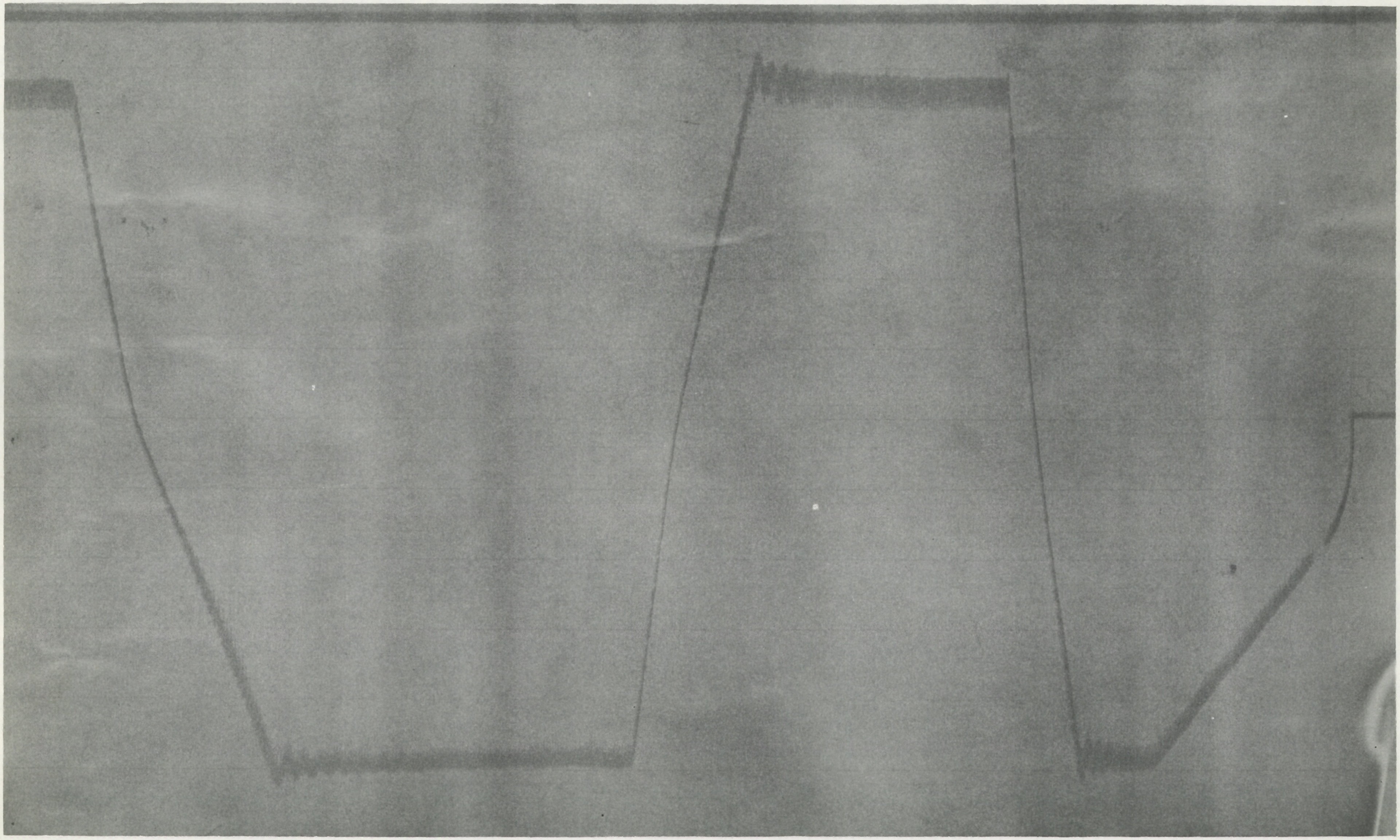

Fig. 4.4b Deceleration and Acceleration - 6-pole stator - Phase-to-Phase Voltage = 160 V, 200 V, and 0.V. (friction only).

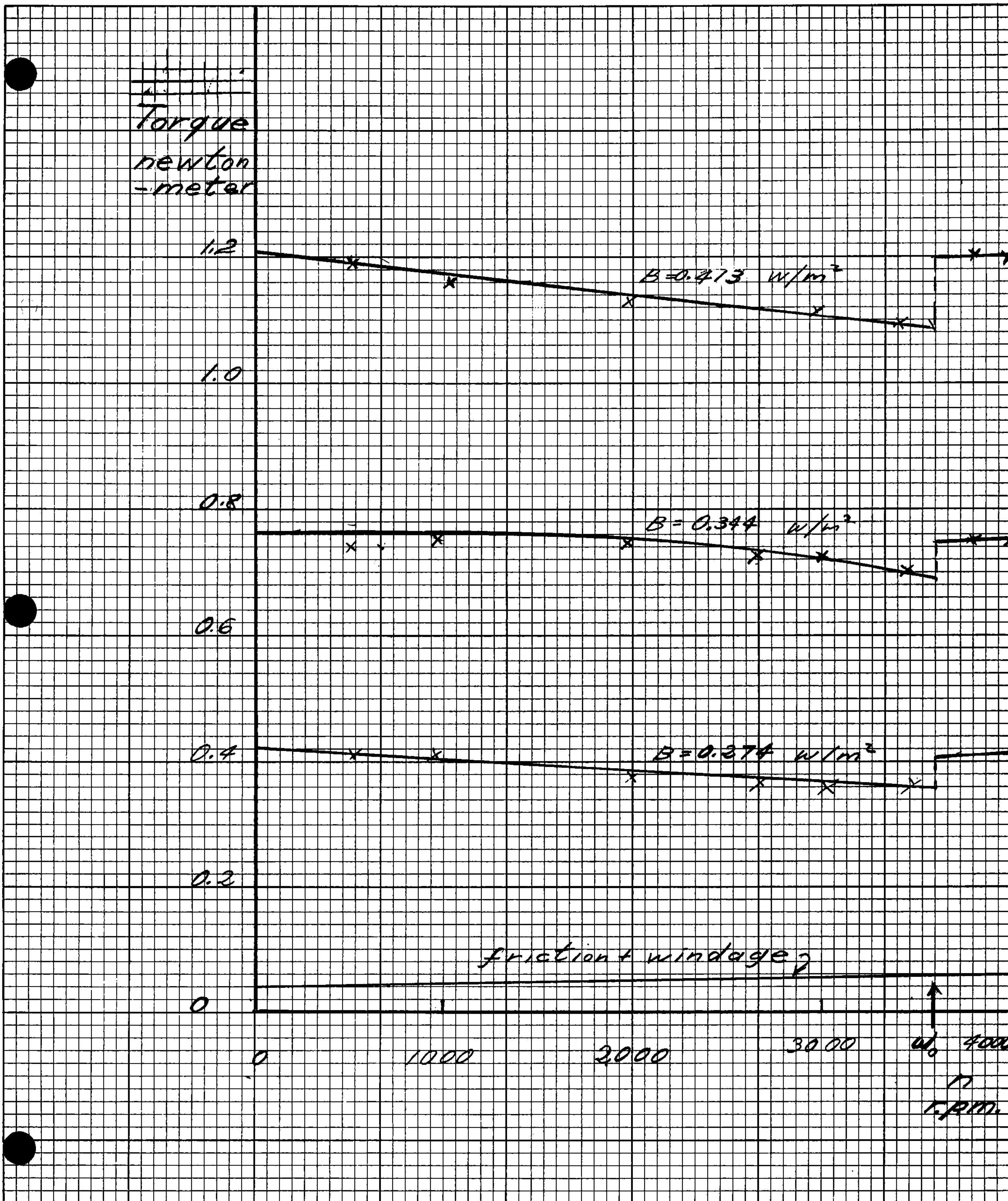

Fig. 4.5a Torque Speed Variation - 2-pole Motor

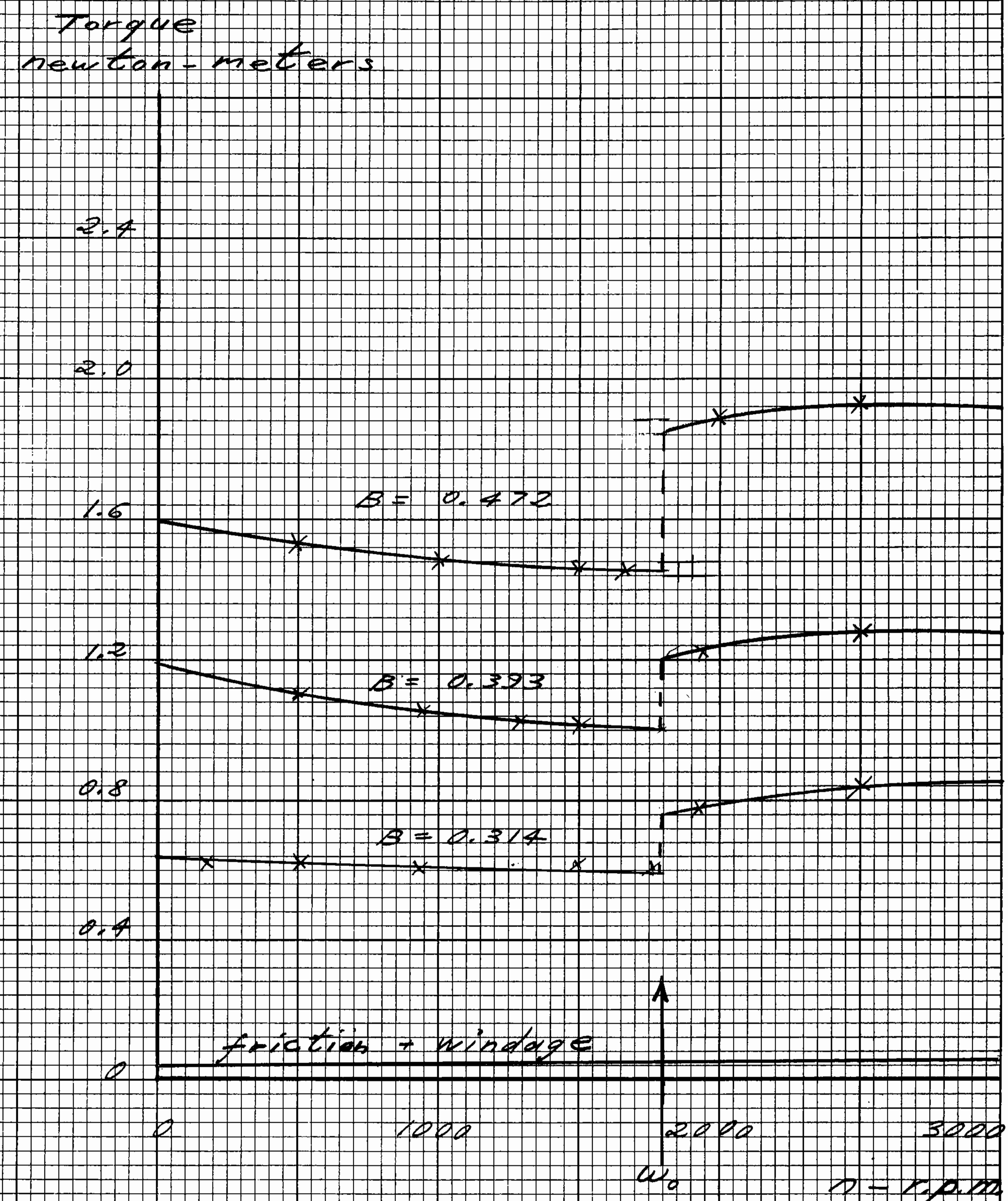

Fig. 4.5b Torque Speed Variation - 4-pole Motor

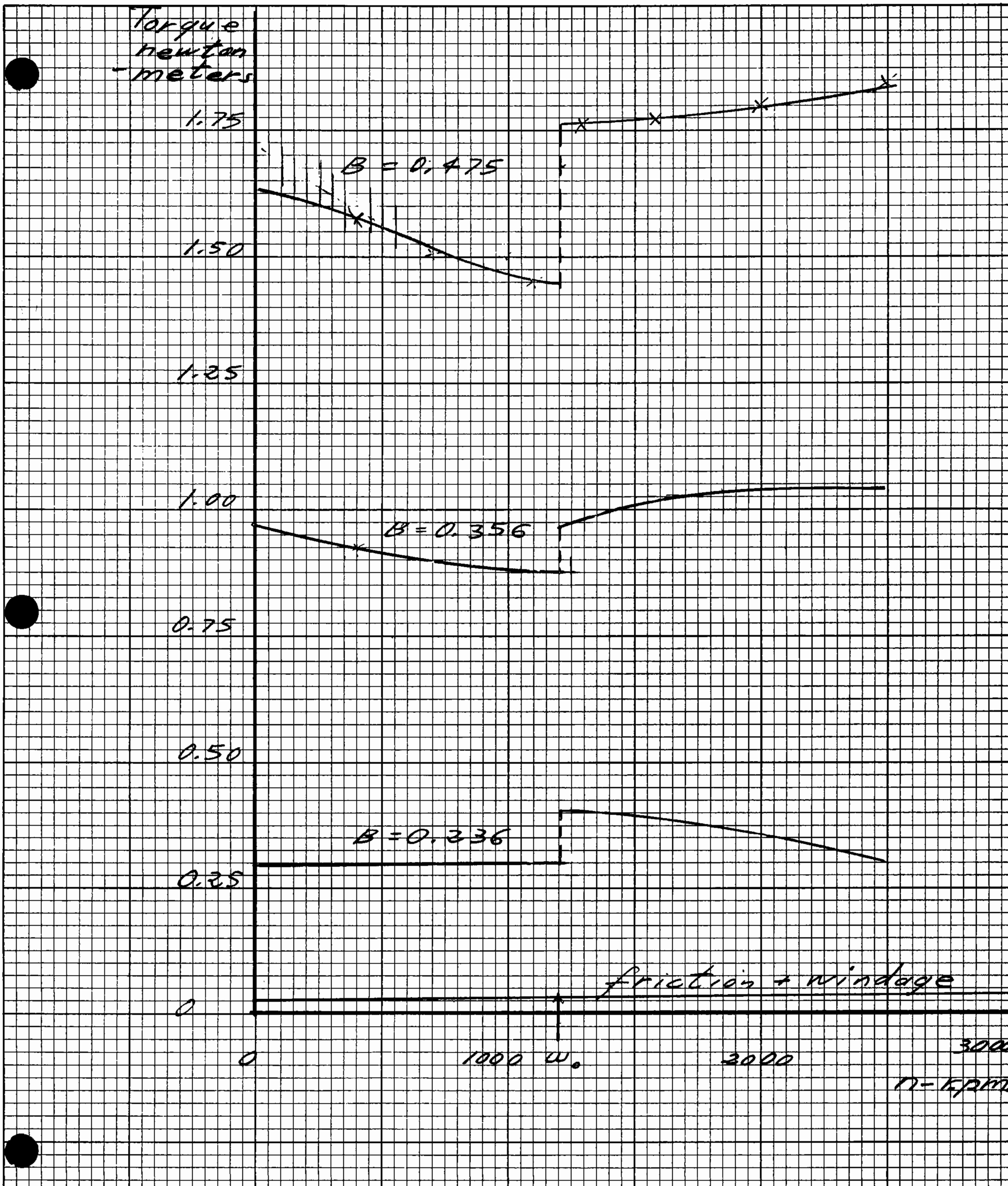

Fig. 4.5c Torque Speed Variation - 6-pole Motor

The second noteworthy feature, namely, the sudden increase in the torque required to drive the motor at a speed just above synchronism over that supplied by the motor below synchronism may only be attributed to high frequency losses caused by tooth pulsations. This will be discussed in greater detail in Section 4.4.

An estimate of what the torque output would be at synchronism without the high frequency effects (since 60 c.p.s. eddy currents have no effect at synchronism) may be obtained by taking the average of the sub- and super-synchronous torques. The comparison of the torque so calculated with that predicted by the theory is shown in Table II. The deviations are rather smaller than those expected in view of the approximations listed in Section 2.3 and the inaccuracy introduced in the determination of the area of the hysteresis loop (Section 3.4). The shockingly large discrepancy at the lower flux densities is not significant since the torque measurements at that level may be in error by as much as 40% due to friction. A rigorous quantitative breakdown of the errors involved is, however, not attempted.

- TABLE II -

Motor	B gauss	A joules/cycle /in^3	Torque Predicted newton-m.	Torque Measured newton-m.	% Error
2 pole	2060	.019	.12	.15	- 18
	2750	.047	.33	.39	- 18
	3436	.09	.63	.73	- 15
	4120	.15	1.02	1.15	- 10
4 pole	3140	.07	.48	.71	- 32
	3930	.13	.88	1.14	- 22
	4720	.21	1.43	1.70	- 16
6 pole	2360	.024	.16	.34	- 50
	2360	.09	.64	.94	- 31
	4720	.21	1.43	1.60	- 10

4.3 Stator Losses.

As with other a.c. motors, the stator losses in the hysteresis motor comprise the copper loss, the eddy current loss and the hysteresis loss. Because the stator is built up of soft steel laminations and the flux density is kept below design levels by the unusually high reluctance of the rotor, the iron losses in the stator are very small, except in case of the two-pole stator.

By far the largest single cause of loss in the motors tested is the copper loss in the stator, since in order to attain suitable air gap flux densities with the very low permeability Vicalloy rotor, it was necessary to run the machine at currents greatly in excess (2-300%) of the design value.

The two-pole stator has relatively the greatest amount of copper, and here the resistance loss amounted to about 25% of the input power at the load required for most efficient non-synchronous operation. In the case of the six-pole stator, where the size of the punchings (intended for a four-pole motor) restricted the amount of space available for the winding, the copper loss exceeded 50% at all non-synchronous operating points. For the purpose of calculating the copper loss the hot 60 c.p.s. resistance of the winding was taken as 1.20 times the cold d.c. resistance[12,28].

It is evident that the prime prerequisite for the efficient non-synchronous operation of hysteresis motors is a low resistance stator winding. This does not mean that the hysteresis motor is necessarily larger than an induction motor of the same rating, since very large power output may be expected from a small rotor. A nearly vertical hysteresis loop is also desirable, for a tilt in the loop decreases the power factor and correspondingly increases the current.

4.4 Rotor Losses.

In the hysteresis motor, as in other types of d.c. motors where the winding is distributed in slots, tooth frequency pulsations[13,14] result in losses due both to high-frequency eddy currents and to parasitic hysteresis loops.

In order to predict the magnitude of these losses, the relative maxima and minima in the flux density directly opposite the stator slots and teeth must be known. This information is however even more difficult to obtain experimentally than the high frequency losses themselves, since the percentage variation in B is closely dependent upon the extent of penetration into the rotor. A rather coarse estimate of the effect of slots on the air gap flux density may be made by assuming that the flux density varies linearly between the minima and maxima (Fig. 4.6b). The total flux per tooth crossing the gap may then be equated to the ideal distribution (Fig. 4.6c) computed by Carter[15,16].

Thus the flux per tooth, on the basis of the distribution shown in Fig. 4.6b, is:

$$(B_{max} - \frac{\Delta B}{2})(s + t)$$

where s = slot width

t = tooth width

This must also be equal to the flux per tooth calculated from the Carter distribution:

$$\frac{\phi_p}{n} = B_{max}\, x$$

where n is the number of teeth per pole

x is the Carter equivalent tooth width

Then $$B_{max}\, x = (B_{max} - \frac{\Delta B}{2})(t + s)$$

$$\frac{\Delta B}{B_{max}} = 2\left[\frac{(t + s) - x}{t + s}\right]$$

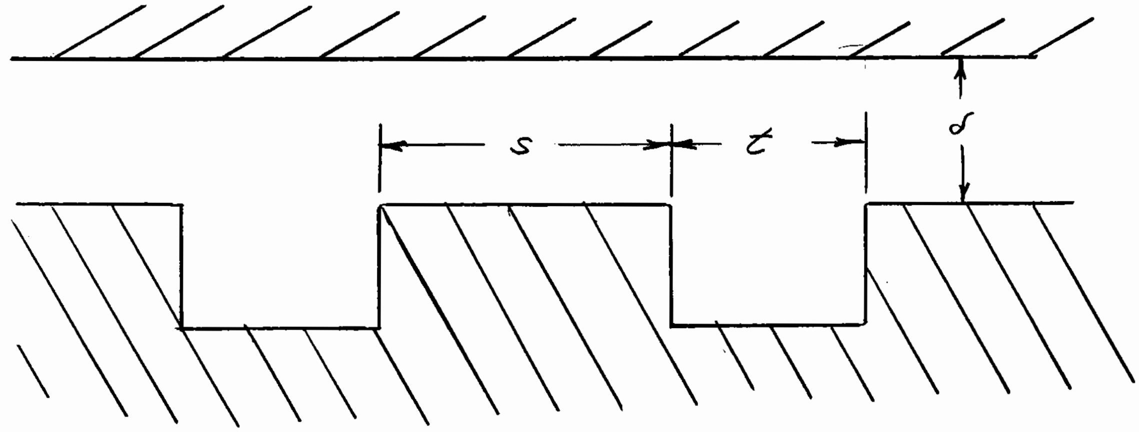

Fig. 4.6a Slot Structure.

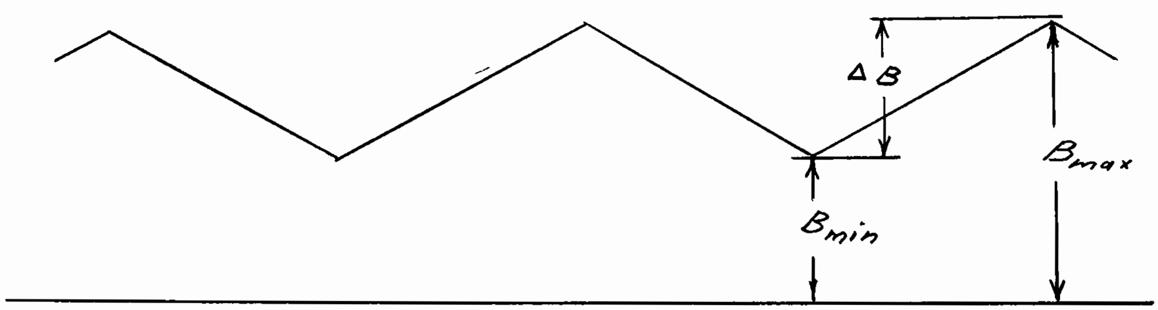

Fig. 4.6b Linear Flux Variation.

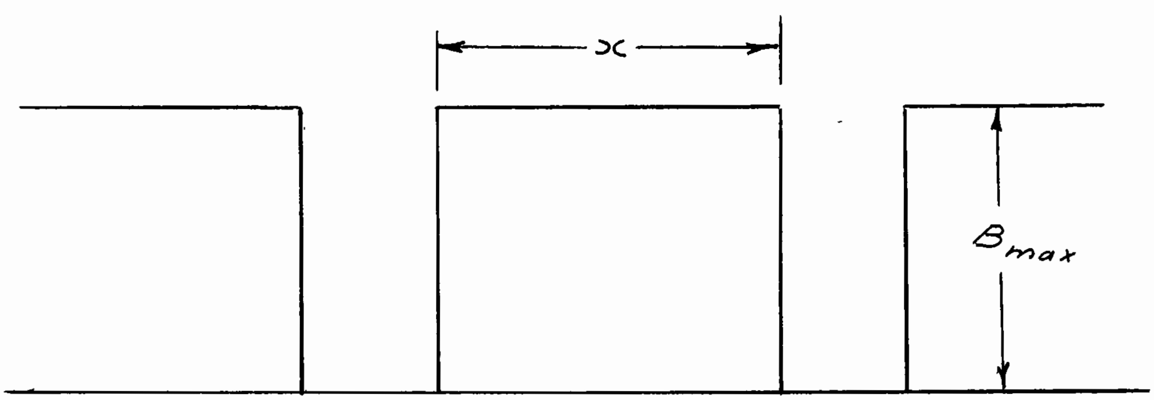

Fig. 4.6c Carter Distribution.

But x = fs, where f is a coefficient chiefly dependent upon the ratio of the slot width to the air gap.

$$\therefore \frac{\Delta B}{B_{max}} = 2\left[\frac{1 - f}{\frac{t}{s} + 1}\right] = 2\left[\frac{1 - 0.43}{1 + 2.50}\right] = 0.33$$

When the variation in flux density was actually measured by means of .250", .070" and .018" wide single turn search coils laid in shallow grooves on the rotor surface, the ratio was found to be closer to 45%, and slightly dependent upon flux density. The signal from the probes was of the order of a few millivolts, and elaborate shielding would be required for precise measurements. The instantaneous flux variation on the surface of the rotor is plotted in Fig. 4.7 for the four-pole stator; the dips are not nearly as large as those shown by Roters[17]. Furthermore, the variation must decrease rapidly with depth of penetration because of the low permeability of the rotor.

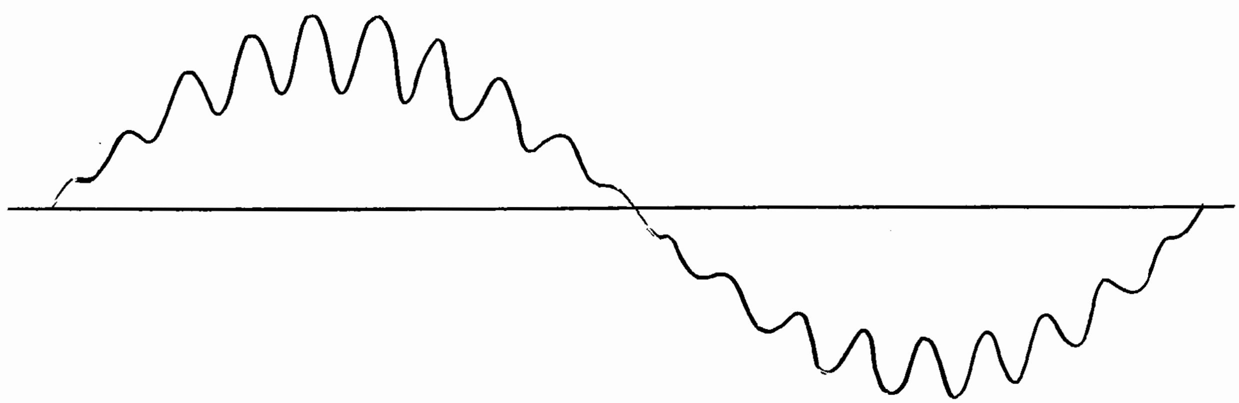

Fig. 4.7 Tooth Frequency Flux Variation - 4- pole Motor.

Both Teare[3] and Roters[4,17] conjecture that the major part of the high frequency losses is due to excursions inside the main hysteresis loop which tend to reduce its effective area. The effect of such loops, referred to as parasitic, subsidiary, or displaced loops, has been studied in some detail by Spooner[18,19], who gives numerous empirical formulae determining the parasitic losses in terms of the maximum flux density, the number, displacement and relative size of the displaced loops, and a constant depending on the material tested. These formulae are unfortunately difficult to apply, not only because the flux distribution is only guessed at, but also because suitable constants are available only for the standard grades of electrical sheet steels.

Spooner's results show, however, that when the rotor is made up of laminations thin compared to the tooth width, the eddy current losses are only a small fraction of the total high frequency loss. It will be shown that in the present instance the total high frequency losses are proportionally much smaller than those encountered by Roters. It seems therefore reasonable to assume that in solid rotor machines the tooth frequency eddy currents are largely responsible for inefficient operation.

As mentioned in Section 4.2, the parasitic losses may be calculated directly from the difference between the sub- and super-synchronous torques at constant air gap flux density. This difference, multiplied by the synchronous speed ω, is in fact just twice the power consumed by the subsidiary loops, which itself is proportional to the speed. It may be seen from Fig. 4.5 that the loss varies between 8 and 20% of the output, depending on the flux density and the stator used.

In order to ascertain the effect of the length of the air gap on motor performance, the rotor was ground down ten thousands of an inch. This increased the length of the air gap by 70%, from .016" to .026".

12% more current was required to attain the same flux density with the larger air gap, increasing the copper losses by 25%. This effect was however compensated by an 8% to 12% increase in the output torque, which may be attributed to lower tooth frequency losses. As shown above, the longer air gap decreases the flux variation opposite the slots and increases the effective area of the hysteresis loop traversed by the rotor material.

The magnitude of the gain and that of the loss was practically the same in the range of frequencies tested. Thus, within certain limits the length of the air gap is not a critical factor in determining the overall efficiency of the hysteresis motor.

4.5 Efficiency.

The constant output torque feature of the hysteresis motor signifies that the theoretical efficiency of the motor is proportional to the speed; the stator has no way of knowing whether the homogeneous rotor is moving or not. Thus, in order to effect comparisons it is advantageous to refer the efficiency to synchronous speed by multiplying it by (1-s), though the value so calculated does not necessarily correspond to the maximum efficiency obtainable at synchronism.

Fig. 4.8 shows the variation in electromagnetic efficiency (friction discounted) with flux density. At first the efficiency increases rapidly as the flux density progresses beyond the first bend in the magnetization curve, thus increasing the power factor, then it attains a plateau where both the output (area of the loop) and the major part of the losses (I^2R) increase approximately as the square of the current.

The customary increase in efficiency with the decrease in the number of poles is more marked here because of the dominant role played by the copper losses. As shown in Table 3, the friction and stator losses remain small in all cases, and the rotor loss depends mainly on the flux density.

The maximum output power obtainable from the test machine is limited only by the rise in stator temperature, since the rotor is not likely to

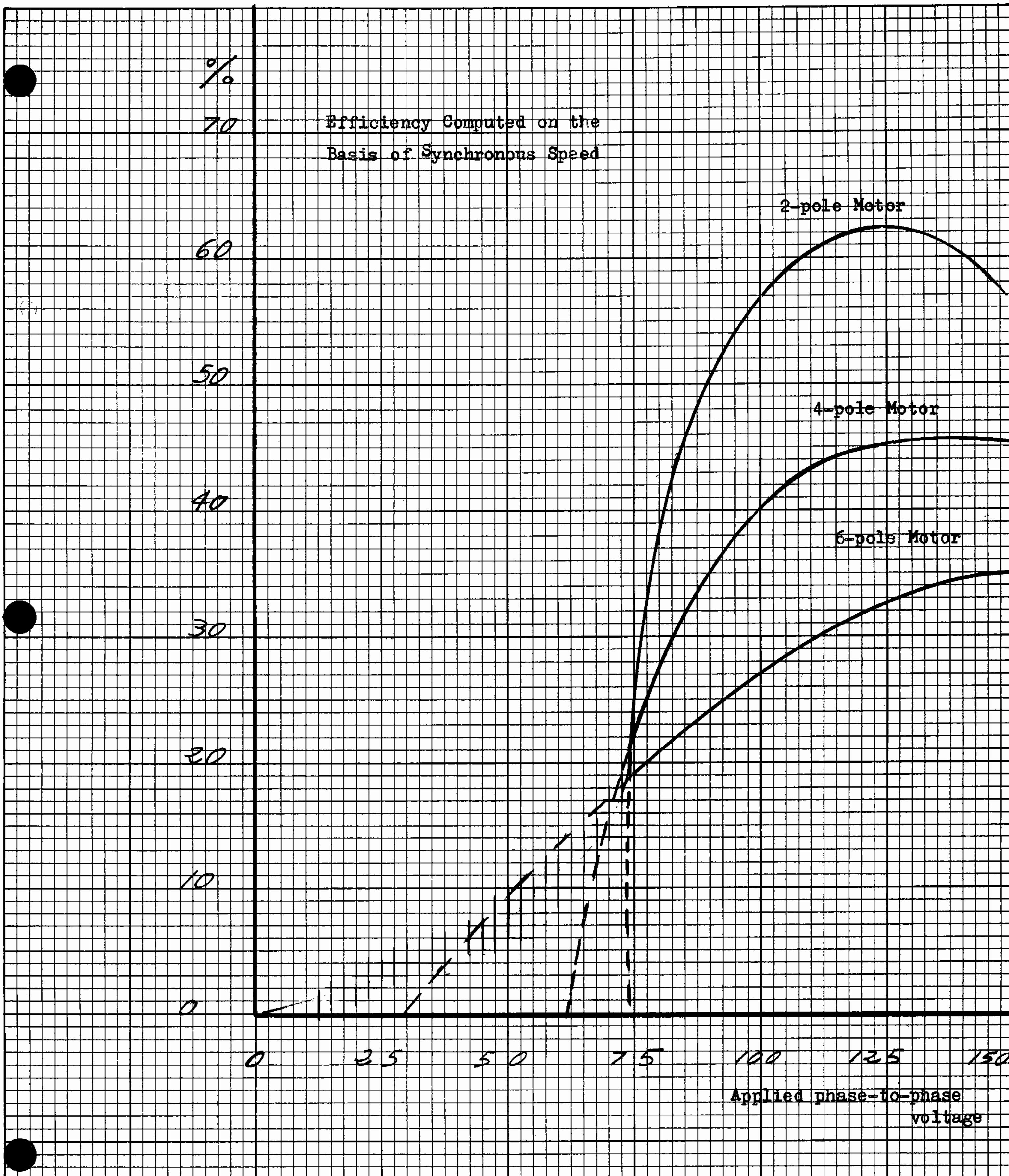

Fig. 4.8 Variation of Efficiency With Voltage - Asynchronous Performance.

- TABLE III -

Details of Losses

Motor	2-pole watts	2-pole %	4-pole watts	4-pole %	6-pole watts	6-pole %
Output	240	54	184	44	130	32
Losses						
Copper	117	26	165	40	214	53
Iron	25	6	8	2	4	1
Friction	23	5	7	2	4	1
Tooth Frequency	18	4	23	5	21	5
Total	423	95	387	93	373	92
Input	443	100	415	100	407	100
Deviation	20	5	28	7	30	8

be damaged by even the very large amounts of heat liberated in it at low speeds. Above and below synchronism rated output could be obtained only momentarily, at the expense of very swift temperature rise.

At peak output, the power factor of all three stators was above 45%, although it varies slightly with speed. This variation and the corresponding 2-3% decrease in current towards synchronism could not be measured with sufficient accuracy, and is probably also due to the presence of eddy currents within the laminations.

4.6 The Equivalent Circuit.

In order to describe the asynchronous performance of the hysteresis motor under all possible conditions, it is desirable to represent its characteristics by means of a simple equivalent circuit. The circuit proposed is shown in Fig. 4.9.

The motor was tested at various flux densities in the 20 to 70 cps frequency range, and the data thus obtained is sufficient to assign values to the components of the equivalent circuit. One set of readings, at a particular flux density and speed, is shown in Fig. 4.10; the equivalent series resistances were obtained from the watt, var and current readings. The reactance is, as expected, strictly proportional to the frequency, and when extrapolated passes through the origin of the plot. It is composed of two parts: X_1, the leakage reactance of the winding, and X_2, the hysteretic reactance due to the inclination of the hysteresis curve.

The resistance also varies linearly with the frequency, but this curve does not pass through the (0,0) point. ωR_2, the frequency dependent part, represents the power per phase developed through hysteresis at synchronism, while the intercept R_1 corresponds to the d.c. resistance of the winding.

The size of the hysteresis loop of Vicalloy does not unfortunately vary exactly as the square of the current, nor does the inclination (permeability) of the hysteresis curve remain constant. Thus both R_2 and X_2 are functions of the air gap flux density, i.e. of the current, and the circuit is not linear. The restricted usefulness of non-linear equivalent circuits need not be emphasized.

More elaborate equivalent circuits include the effects of eddy currents, harmonics and tooth frequency pulsations; a thorough discussion is given in reference 5.

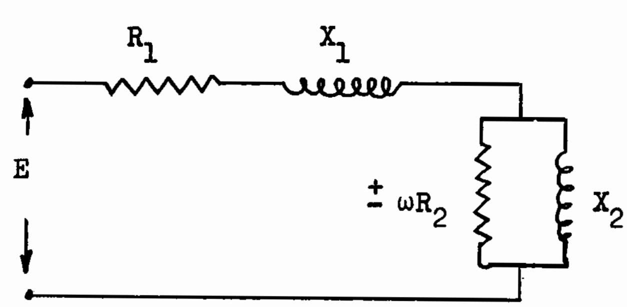

Fig. 4.9

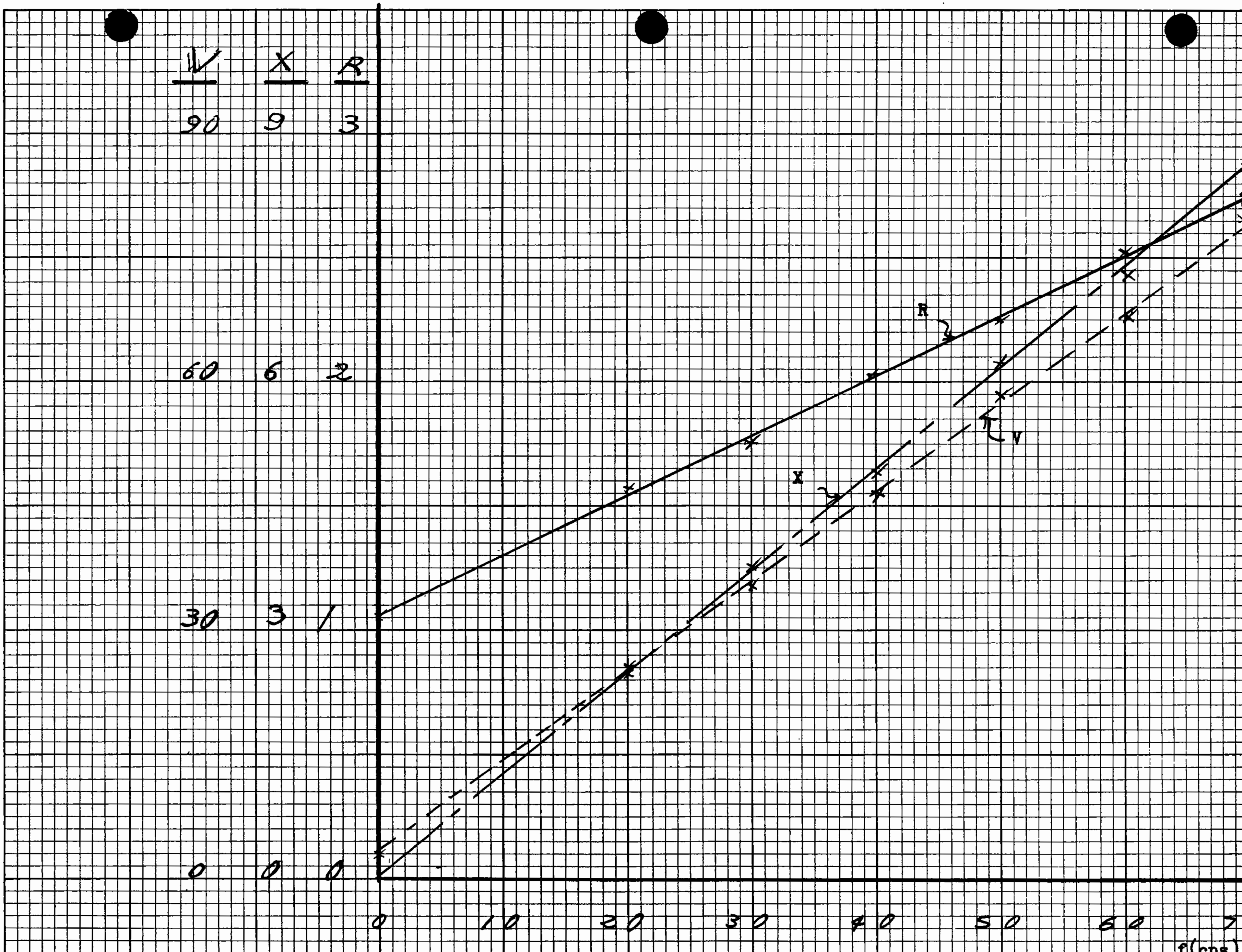

Fig. 4.10 Variation of Resistance and Reactance with Frequency (frequency in cps) Constant Flux Density

CHAPTER V

Synchronous Performance

5.1 Vector Diagram at Synchronism.

At synchronism the rotor of the hysteresis motor behaves essentially like a permanent magnet; the various portions of the rotor are magnetized to a constant flux density, depending on their position relative to the stator flux-wave at the moment dynamic equilibrium was attained. The sinusoidally distributed remanent rotor magnetization may be observed by turning off the stator excitation and connecting an oscilloscope either to a search coil mounted on the stator or to part of the stator winding itself while the rotor is still moving. Care must however be taken to use a switch which will break all three phases within a time interval very short compared to a rotor revolution, otherwise the rotor will remain unsymmetrically magnetized.

Fig. 5.1 is a vector diagram showing the spatial phase relationship of the fundamentals of the various electromagnetic quantities at synchronism. The phasor E represents the applied voltage - the resistance and reactance drop through the stator have been omitted for the sake of simplicity - which rotates counterclockwise at synchronous speed. The solid lines represent the distribution of e.m.f., current, m.m.f. and flux at the moment the rotor attains synchronism, and is delivering full load torque. The radial component of the magnetomotive force, H_r, is in space (and therefore time) phase with the current vector I, and induces a flux density B (only the radial component is of the interest) in the rotor which lags H_r by the hysteretic angle α (value for the combination of rotor, stator and

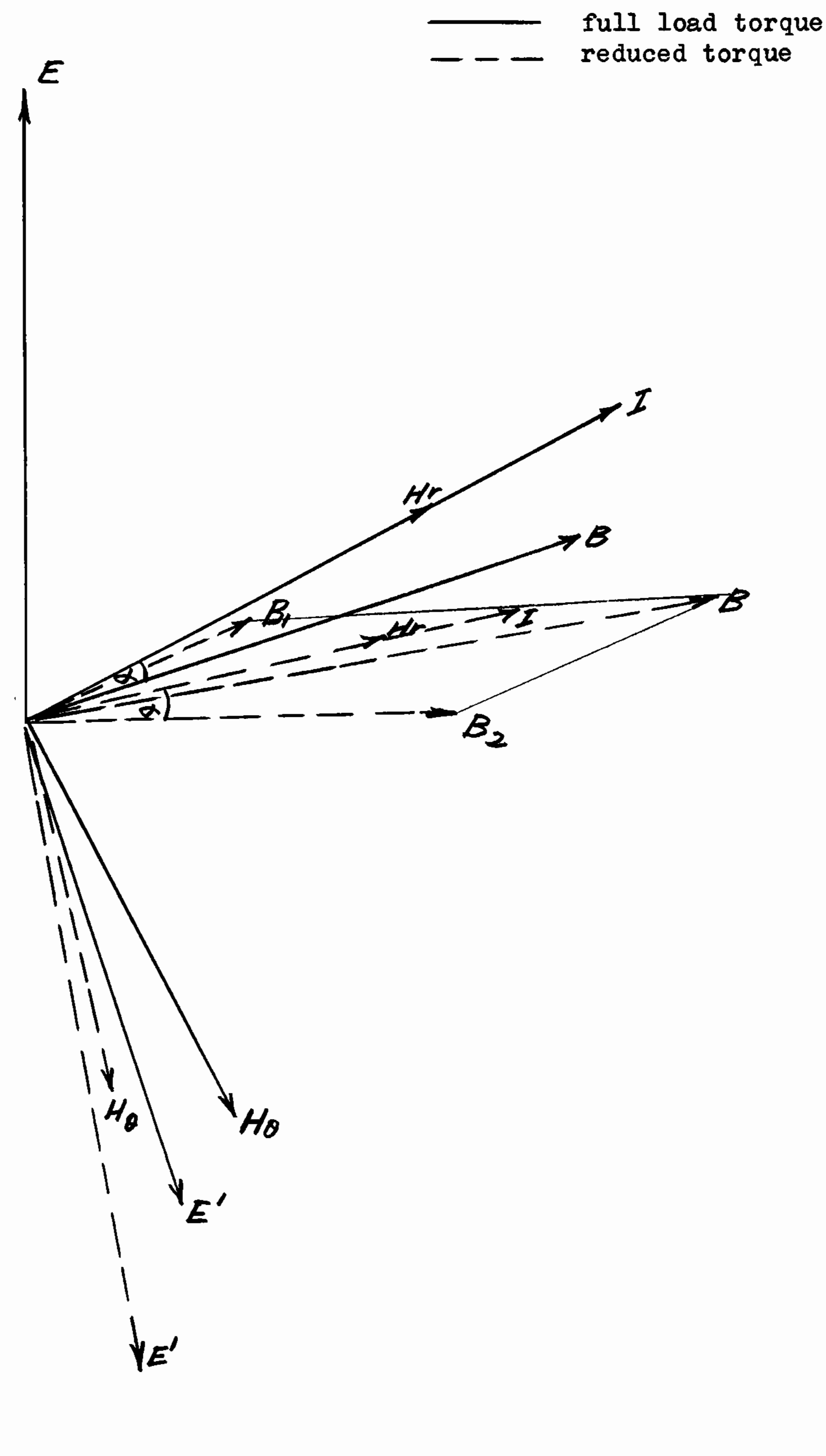

Fig. 5.1 Space Vector Diagram-Synchronism.

air gap). This in turn gives rise to a counter e.m.f. E' lagging B by 90°, and the vector sum of E and E' must be such as to correspond in phase to the current vector. As shown already, a tangential component of the m.m.f. must exist at 90° to the radial component, and it is the scalar product of the tangential component H_{θ} with the flux density B (really B_r) which determines the torque.

When the torque is reduced, the situation is complicated by the effect of residual magnetism in the rotor. This state of affairs, with the applied voltage unchanged, is shown in broken lines in Fig. 5.1. The decrease in the torque demanded allows the rotor to pull in closer to the stator e.m.f. wave, while the current and power factor decrease in order to reduce the power supplied to the rotor. The radial component of the flux density B_2 still lags the m.m.f. by α, but now there exists also another component, the residual induction B_1, which has been advanced in space by the change in the rotor angle. This residual induction disappears only when an alternating m.m.f. wave sweeps it away, i.e. the rotor drops out of synchronism. The resultant of the two components of radial flux density is B, and E' lags B by 90°. Since the angle between E and E' is greater now than before, the current and power factor are smaller, as expected from power considerations. The decrease in torque results from the diminution in H_{θ} and the increase in the angle between B and H_{θ}, despite the slight increase in B.

5.2 No-load Behaviour.

In the ideal motor, the power factor should reach zero precisely when the torque at the shaft vanishes and the angle between B and H_{θ} is 90°; beyond this point, generator action takes place. The departure of the real motor from the ideal is shown in Fig. 5.2, and is due to the various losses.

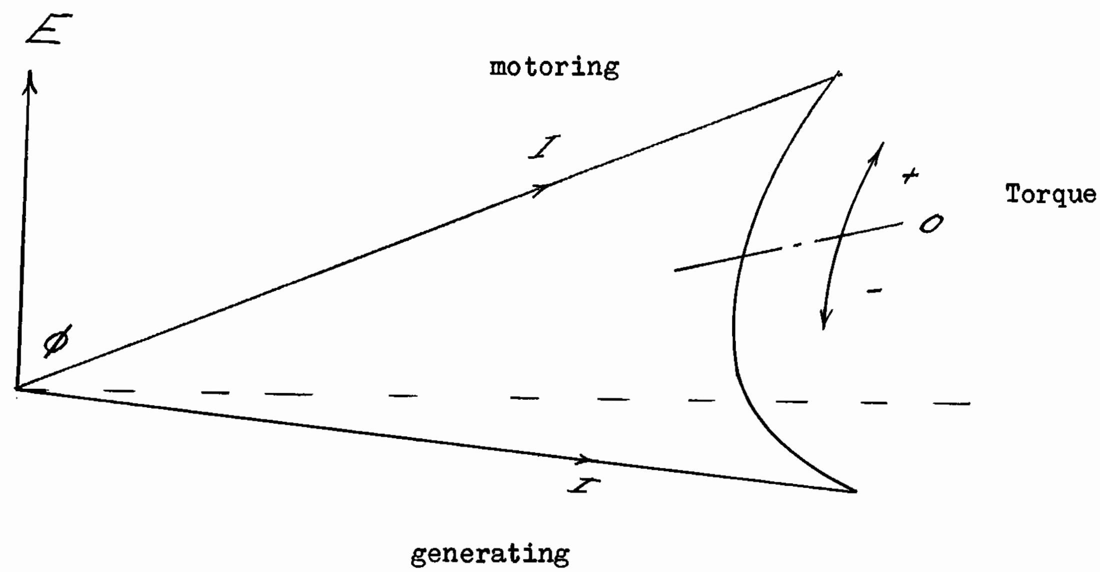

Fig. 5.2a Current Locus at Synchronism.
2-pole Motor - B = 0.344 webers/m^2.

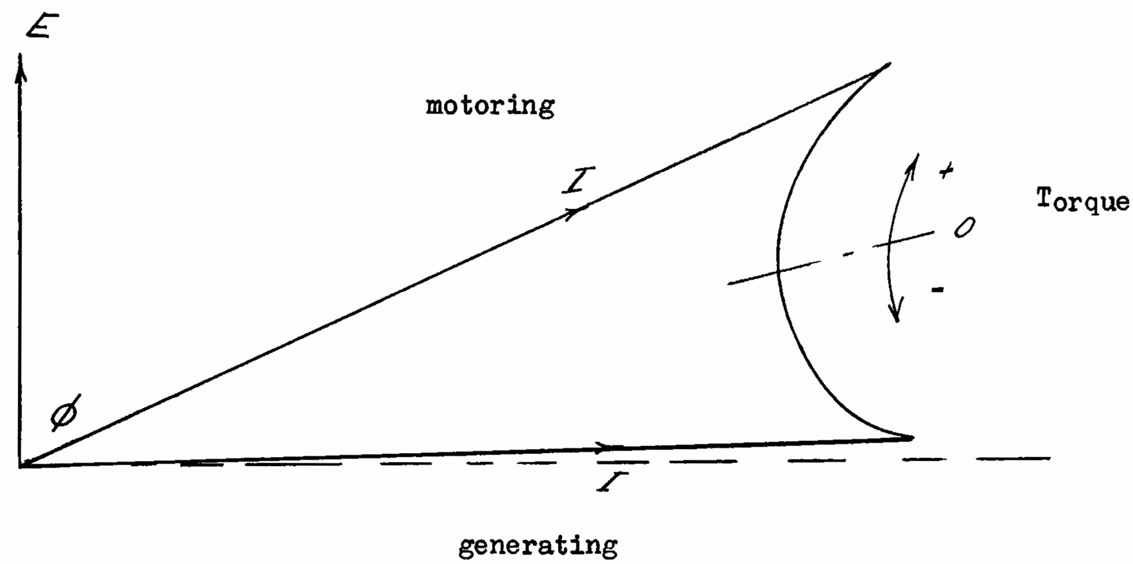

Fig. 5.2b Current Locus at Synchronism.
6-pole Motor - B = .412 webers/m^2.

Thus, an alternative determination of the high frequency losses is possible at synchronism, provided all other losses are known. When there is no external load on the motor, the principal losses are the copper loss, the friction loss, the ripple loss and the iron loss. Table IV shows the data necessary to determine the high frequency losses in this manner, and a comparison with the figures obtained in the previous chapter. The discrepancies are not too disquieting since the no load input depends on the past history of rotor, as shown in the previous sections.

- TABLE IV -

	2-pole watts	4-pole watts	6-pole watts
Input at Synchronism at zero Torque Output	156	144	143
Copper Loss	83	109	124
Iron Loss	25	8	4
Friction Loss	23	7	4
Stator Losses (Incl. Friction)	131	124	132
Synchronous Tooth Frequency Loss	25	20	11
Asynchronous Tooth Frequency Loss (Table III)	18	23	21

Because of the relatively high currents exacted by the low rotor permeability at synchronism the efficiency of the hysteresis motor decreases with the load. The efficiency curves of the various stators are plotted in Fig. 5.4 in order to permit comparison with the efficiency attained with the help of pulsing, as discussed in the next section.

5.3 Pulsing.

The part played by remanent magnetism in maintaining the rotor flux density may be turned to great advantage by momentarily pulsing the rotor at a voltage and current much higher than its normal rating. The duration of the pulse need not be much longer than the period of a single cycle, although in the present experiment a manual switch was used. This procedure results in a considerable improvement in efficiency, due mainly to the fact that once the required radial flux density has been established, little current is needed to maintain it.

Fig. 5.3 is the relevant vector diagram. The situation represented by the solid lines is the same as that shown in Fig. 5.1; the rotor has just pulled into synchronism. Next, the motor is pulsed to a level approximately twice its normal operating voltage, and a corresponding increase in current, m.m.f. and flux density ensues (dotted lines). Although the rotor is displaced relative to E, the residual induction remaining from before the pulse is neglected since it is small compared to the new flux density. At this point the power factor is low, because the mechanical load has not been increased, and the torque is only a fraction of what the motor could momentarily develop.

When the applied voltage is restored to its former level (broken lines) the rotor drops back, and with it the large residual induction B_1. In order to produce the necessary m.m.f. to interact with the flux density, only a small current is necessary, which however induces B_2. The resultant of B_1 and B_2 is B, and B is necessarily of the right magnitude and phase to generate E', which in conjunction with E determines I. Although now I is indeed small, it is at a favourable phase angle; the angle between H_θ and B is much smaller than before, and compensates for the decrease in the size of H_θ (B is about the same as before the pulse).

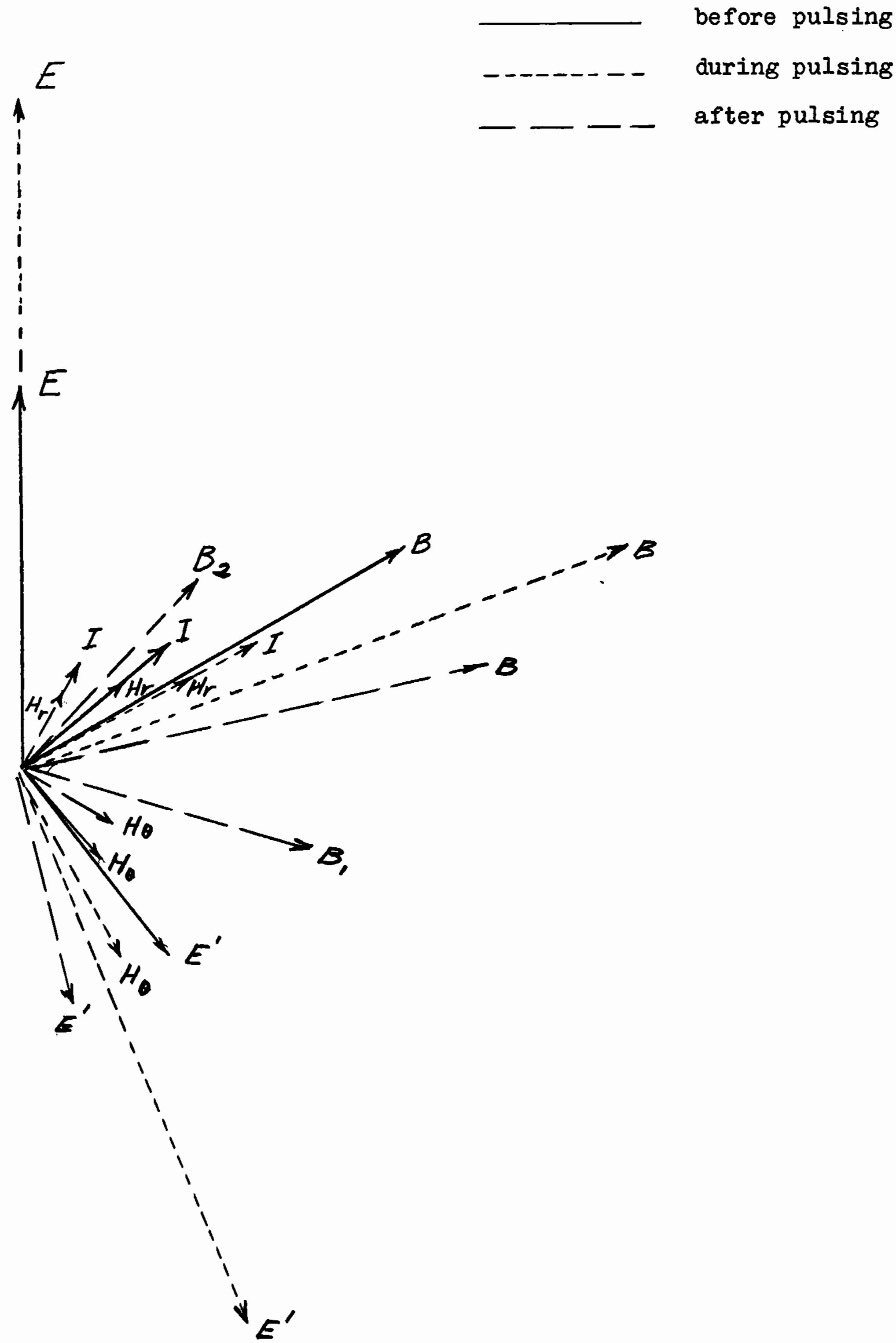

Fig. 5.3 Vector Diagram—Pulsing at Synchronism.

It should be pointed out here that the remanance as mentioned above is not quite the same as that customarily specified in connection with permanent magnets[20], since the current goes down to zero only at certain discrete points corresponding to the number of poles in the stator winding. At other points the flux density merely moves back along the hysteresis curve as far as the current at the point ahead of it by the angle α will permit it to move. This augurs difficulties, which will not be confronted here, for the precise theoretical prediction of the effects of pulsing.

Despite the somewhat abtruse electromagnetic adjustments which take place in the process just described, the gain in efficiency is tangible enough. Curves of the efficiency versus the torque, after pulsing at synchronism, are displayed in Fig. 5.4. While it must be kept in mind that these values apply to the electromagnetic torque, and that if the friction loss were subtracted the efficiency would be 3-6% lower, the efficiency is nevertheless already in the induction motor range.

The motor tested could be used at high efficiency near rated load (stator) only intermittently, for periods up to 30 minutes, but the residual magnetism was tested at lower flux densities and found unchanged during intervals of up to 5 hours.

The efficiencies depicted above are in some cases superior to those claimed by Roters[6], who also pulsed his motors. This would seem to indicate that closed stator slots are not essential in laminated hysteresis motor design, and that the costs involved in winding such slots could be turned to better profit elsewhere.

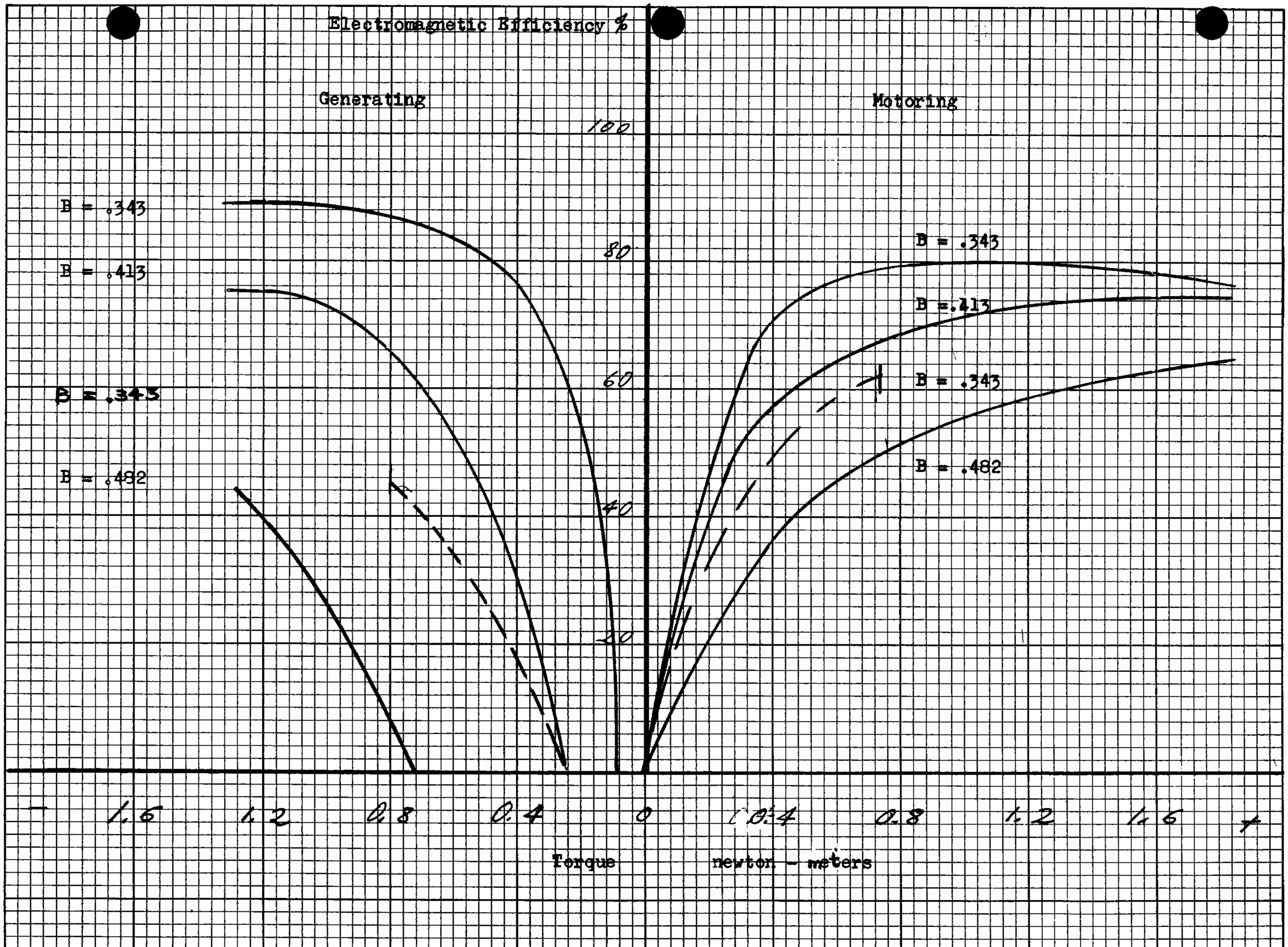

Fig. 5.4 Efficiency — Pulsing — 2-pole Motor

—— Pulsed to .660 webers/m^2
- - - Unpulsed

CHAPTER VI

Conclusions

6.1 Characteristics of Test Machines.

The three hysteresis motors tested are capable of producing 45 - 55% of the output of induction motors of the same frame size continuously, and 75 - 85% intermittently, at electromagnetic efficiencies ranging from 60% at subsynchronous speeds to 84% at synchronism after pulsing. The power factor varies from 40% to 90%, while the variation in torque, due to eddy currents, is restricted by the presence of laminations to about 12% between standstill and synchronism. The asynchronous torque output of the machines corresponds to the theoretically predicted torque within 10 - 30%, where the lower limit indicates the applicability of the theory, while the upper limit reflects the minimum accuracy of the measurements.

The greatest single cause of inefficiency is the copper loss in the stator. This accounts for over 45% of all the losses. Doubling the amount of copper in the stator of the four-pole machine would raise its efficiency by about 16% and also increase the maximum continuous output considerably.

The next important offender is the high frequency loss due to pulsations at tooth frequency. This loss however does not seem as large as hitherto thought unavoidable; apparently high frequency eddy current losses were erroneously ascribed to subsidiary hysteresis loops. Thus laminating the rotor seems as effective a solution as some of the more drastic measures applied previously.

Iron losses in the stator are slight since the machines are perforce always run well under the rated air gap flux density.

The higher efficiencies and power factors could be attained only by pulsing the stator at close to twice rated voltage. This causes remanent induction to induce a counter e.m.f. which restrains the current; at the same time it reacts with the m.m.f. to develop torques higher than otherwise obtainable at the same terminal voltage. A qualitative treatment by means of vector diagram is sufficient only to outline the principal features of the method and is not really suitable for quantitative predictions. Neither is the simple equivalent circuit derived in Section 4.6 easily adaptable to represent synchronous operation.

6.2 Scope for Further Research.

If a truly accurate solution for the torque output of the hysteresis motor is desired, especially at higher flux densities, the first step will be evidently to tackle the problem in its full non-linear complexity[21]. While the more elaborate analogue computer installations can be used to solve partial differential equations, any problem where time is not the only independent variable causes hideous complications[22]. Furthermore, two-valued functions, such as a hysteresis curve, are rather difficult to generate.

Any of the several numerical methods[23] (e.g. the Runge-Kutta method) for solving partial differential equations may be programmed for iterative solution on a digital computer, and this would perhaps be a more practical approach to the problem. Scanners are now available to convert photographs of the hysteresis loop of the rotor material at various flux densities directly into a form suitable for reference by the computer. It must however be noted that at the present time, and taking into consideration the size of the hysteresis motors now being built or likely to be built, a precise calculation by means of either analogue or digital computers of the torque developed by such motors could hardly be considered more than a somewhat arduous academic exercise.

Once the problem has been solved, even approximately as in Chapter II, it may well be worthwhile to simulate the various parameters on an analogue device or to feed the data and method of solution into a digital machine in order to determine the most economical design. This is becoming common practice in design offices, and would be of particular value in hysteresis motor design where rotor materials vary so widely in price and magnetic properties.

A more detailed study of pulsing, especially with regard to the permanence of the remanence of various materials under different conditions of torque oscillation and vibration, may lead to some ingenious method of taking advantage of the high efficiencies obtainable in this manner.

Comprehensible data on hysteresis losses with high frequencies superimposed on a fundamental is still not available for hard magnetic materials. Apparatus similar to that described in Section 3.4 could be used to obtain it, although a larger outer diameter and cross-sectional area in the toroid and more turns on both the primary and the secondary windings would be preferable. A motor-generator set or frequency multipliers could supply the high frequency, which, in order to reproduce conditions in the rotor, would have to be amplitude modulated by the low frequency. The main problem is that this source would have to be capable of passing the very large fundamental as well. An alternative would be to introduce the low and high frequency components of the m.m.f. in separate windings, and to use wattmeters to measure the loss.

Before deciding however whether practical considerations justify elaborate experiments to turn already known principles into four figure quantitative data, it may be well to cast about for possible fields of application. This forms the subject matter of Section 6.5.

6.3 Principles of Design.

As seen in Section 6.1, the simplest way to increase the efficiency of a practical hysteresis motor is to increase the volume of copper in the stator. Because of the high present cost of materials suitable for rotor construction, the most economical design has a much larger ratio of copper to rotor material than an induction motor of the same rating. The relative rise in efficiency is more rapid than the increase in the amount of copper, because the high currents now permissible entail higher flux densities, where the hysteresis curve of most materials is less tilted and the power factor consequently more favourable. Of course, the rotor must never be driven into saturation; according to Brailsford[29], for all materials there exists a point of optimum excitation, beyond which the rotational hysteresis loss actually decreases and eventually reaches zero.

While with laminated rotors the high frequency loss is not too serious, it pays nevertheless to devote care and attention to the design of the slot structure and the ratio of the width of the slots to the air gap. The rotor itself, if it consists of a low permeability alloy such as Vicalloy, accounts for by far the major portion of the total reluctance of the magnetic circuit. It is therefore permissible to provide air gaps longer than those customary without significantly increasing the number of ampere-turns required. Apart from promoting a more uniform flux density distribution, the long air gap is also conducive to better ventilation.

The optimum thickness of the rotor laminations may be determined either by the amount of torque variation which may be tolerated at sub-synchronous speeds, or by the high frequency eddy currents depending on the slot pitch.

The ideal rotor material should have a hysteresis loop symmetrical about both the H and the B axes, and preferably be elliptical in shape.

A rectangular loop would give rise to high frequency components in the current, with the attendant losses. The area of the loop determines the torque available for any given m.m.f., while the optimum ratio of the maximum flux density to the m.m.f. (permeability) is a question of the relative costs of rotor material and copper. Very tall, thin loops (high remanence, low coercive force) require excessive amounts of iron in the stator, but since the saturation flux density of prime grade steels is high, this does not constitute a common limitation.

As long as high loss materials are available only at their present price level, the most economical design is a thick walled cylindrical shell. For special applications, where large output torque per unit volume is required, the solid cylinder is indicated.

Wherever a motor may be called upon to operate at synchronism for periods of several hours at a time, it may be economically justifiable to incorporate a device which will apply a higher than normal operating voltage to the winding while or just after the motor comes up to speed. With three phase motors, the winding may be switched from delta to star connection after the rotor has locked into synchronism, or capacitors may be momentarily inserted into the circuit to raise the current.

6.4 Magnetic Materials Suitable for Rotor Construction.

Although any ferromagnetic material may be incorporated into the rotor of a hysteresis motor, until quite recently materials developed for permanent magnet applications were almost exclusively used. In the past few years however one or two companies have marketed alloys primarily designed for hysteresis motors. The great demand for ferrites has also helped to promote the development of potentially interesting hysteretic properties. The materials now available are briefly reviewed in this section.

The oldest and perhaps most popular among the permanent magnet steels are the Alnicos[24,30,31], consisting of iron, nickel and aluminum in various proportions. These alloys exhibit extremely high hysteresis losses, but also require large magnetizing forces to take full advantage of this feature. Alnico rotors are generally cast in a fairly thin shell, with a soft magnetic material such as low carbon sheet steel to back it up and to supply a low reluctance path to the flux. Mechanically the Alnicos are very hard and brittle, and can be machines only by grinding. Alnicos cannot be rolled or extruded, and although their resistivity is much higher than that of ordinary steels, it is not sufficient to effectively limit eddy currents.

Vicalloy[9] (vanadium, nickel and iron) is a very convenient material to work with inasmuch as it is machinable and available in strip form, and does not require excessive magnetizing forces. At low flux densities the shape of the Vicalloy hysteresis loop is almost elliptical, but with considerable tilt to the curve, while near saturation it yields an equivalent power factor much closer to unity. Thus a compromise must be reached between the volume of rotor material needed and the power factor of the motor.

Remalloy[24] is a very promising material with magnetic and physical properties much like those of Vicalloy. It contains 17% molybdenum, 12% cobalt, and 71% iron, and is cheaper than materials with a higher cobalt content.

A new material developed especially for hysteresis motor applications is P-6[25], an alloy of cobalt (45%), nickel (6%), vanadium (4%) and iron (45%). P-6 is most efficiently used at magnetizing forces of about 60 oersteds, which is almost attainable with normal stator windings. Had the motors tested been made of P-6 instead of Vicalloy, the subsynchronous torque output may have been raised by a factor of 2.5 at rated current. P-6 exhibits an almost vertical hysteresis curve, and relatively high residual induction indicates that pulsing could be applied to advantage. This material is machinable and may be hot or cold rolled before the final aging treatment, which takes place at a very elevated temperature.

Ferrites[26] are now available at a wide variety of magnetic chacteristics, which range from tall thin loops to extremely wide squat ones. The cost of these materials is low compared to that of the alloys described above, and their resistivity is sufficiently high to eliminate eddy current losses almost entirely. Most of the problems arising from the construction of hysteresis motors would likely be mechanical ones, since the ceramics are weak and brittle and may be machined only with the greatest difficulty. Nevertheless a rotor could be made up of rings pressed together on an arbor, provided the speed and outer radius were small enough to prevent disintegration of the material due to centrifugal and vibrational forces. Motors with very low permeability (1-10) ferrite rotors would be particularly suitable for asynchronous constant torque operation, since the large amounts of heat (proportional to the slip) generated in the rotor would not damage the rotor and the design could incorporate a long air gap to act as thermal insulation between rotor and stator.

In Table V the most pertinent properties of the materials discussed are compiled in a form suitable to serve as a preliminary guide in the selection of rotor material for a particular application.

6.5 Applications.

The efficiency of a motor is closely related to the maximum economical size of that design; thus, the hysteresis motor has evolved from clockwork and demand-meter applications requiring only a few watts at 1 or 2% efficiency to the point where, at present, small integral horsepower sizes seem practicable.

- TABLE V -

Properties of Magnetic Materials Suitable For
Hysteresis Motor Construction

Material	Vicalloy	P-6	Alnico II	Alnico IV	Alnico V	Remalloy	17% Cobalt Steel
Manufacturing Process	hot or cold rolled	hot or cold rolled	cast (sintered)	cast	cast (directional)	hot rolled	hot rolled
Price per 100 pounds	650.-	600.-	550.-		590.-	400.-	250.-
Specific Gravity	8.5	8.2	7.1	7.0	7.3	8.3	8.4
Flux Density in Gauss							
at H = 100 oers.	1,600	16,000	450	400	400	1,000	
= 200 "	5,400	17,000	1,000	800	800	2,800	
= 500 "	11,200	18,000	4,000	2,200	2,800	12,000	
= 1000 "	13,000	19,000	10,000	6,600	14,000	15,000	
Hysteresis loss per cycle in joules/cu.in.							
at H = 100 oers.	.02	.35	-	-	-	-	.01
= 200 "	.33	.42	.01	-	-	.07	.28
= 500 "	1.20	.50	.30	.16	.16	1.23	1.00
= 1000 "	1.50	-	2.00	.95	3.80	1.42	1.15

The single phase, shaded pole, self-starting hysteresis motor is indeed particularly suitable for timing mechanisms, and has been used for this purpose almost since the turn of the century. With the advent of various types of automatic controllers, large numbers of such motors came to be used to power recording mechanisms and to trip relays at preset time intervals.

Slightly larger sizes are suitable for turn-tables, motion picture projectors[27], and tape-decks, although in the latter application sub-synchronous operation may be required in order to keep the tape speed, rather than the angular velocity of the reel, constant. Here the constant torque feature affords some measure of protection since in a well designed tape recorder the motor will stall before the tape can break.

In servomechanism applications the hysteresis motor is restricted to the relatively small number of systems where frequency dependent (synchronous) operation is required. Because all of the rotor, rather than just the periphery, contributes towards the torque production, very low inertia, small time constant motors may be constructed.

As mentioned before, one of the most useful features of the hysteresis motor is that no brushes or slip rings are required. This makes the motor ideal for explosive atmospheres, and it should be used wherever synchronous speeds are needed at hazardous locations. No special devices are necessary to protect the motor against stalling; even at standstill the rotor is not likely to overheat sufficiently to ignite the vapours.

It has been seen in Section 6.4 that the hysteresis motor is capable of developing very large amounts of torque per unit volume, and would thus appear suitable for the intermittent duty cycle required in moving mechanical controls or control surfaces in air-borne equipment. Mechanical linkage could convert the rotary motion into whatever type of movement is required, and the motor would function as a sort of long-stroke relay. Although hydraulic motors are capable of a far larger torque-to-weight ratio, they require a pump and compressor generally driven by an electric unit.

In contrast to d.c. excited synchronous motors equipped with amortisseur bars, the starting current of a hysteresis motor is the same as the running current, and there is no sudden spasm when the motor locks into synchronism, even under full load. Furthermore, the apparent synchronizing torque in a d.c. excited or reluctance type motor is greatly affected by the inertia of the connected load, because synchronization must take place within a single half cycle from normal slip speed or not at all. With the hysteresis motor, inertia affects only the total time required to reach synchronism. Gyroscopes, for instance, connected to delicate instruments, may take advantage of the smooth acceleration afforded by the hysteresis motor.

While, all in all, the above list is not too extensive, new applications will no doubt be discovered, and as the art of design progresses, the hysteresis motor will assume an increasingly useful position among the stock of equipment available to the electrical engineer.

APPENDIX

INDUCTION MOTOR — DESIGN SHEET

STATOR Lam No. E-12161	
Diam. ext.	5.75 Square
int.	3.75
Core stack.	2.75
ducts	
Stack. factor	
Iron	24M36
No. of slots	36
Core depth	
Slot depth	
width	
Wdg. area	
Tooth width	
Slot insul.	.020
Wdg. type	Lap
connect.	Y
Slots/ph./pole	6
Turns/coil	10
Cond./phase	240
Cond. width	2#19 HF
depth	
Factor space	
dist.	
pitch	
Pitch coil	1-16
slot	
pole	
Cond. length	
R at 75°	1.18
volts at 75°	
L.M.T.	24.0

ROTOR Lam No. Y-23412	
Diam. ext.	3.724
int.	.75
Core stack.	2.75
ducts	
Stack. factor	
Iron	
No. of slots	45
Core depth	
Slot depth	
width	
Wdg. area	
Tooth width	
Slot insul.	
Wdg. type	S C
connect.	
Slots/ph./pole	
Turns/coil	
Cond./phase	
Cond. width	As slot
depth	
Material	Alum
Conductivity %	
Factor space	
dist.	
pitch	
Pitch coil	
slot	
Cond. length	
R at 75°	
volts at 75°	

NETT. WEIGHTS	
Stator Wdg.	3.50
aux.	
Rotor cond.	.40
ring.	.43
Stator teeth	
core	

MISCELLANEOUS DATA.

AUX. WDG.	
Capacitor	
Wdg. type	
Slots per pole	
Turns per coil	
Conductor	
Coil pitch	
R. at 75°	
Rotor resist.	
Locked, X	
Cap. X	
X.-Xc	
Z	
I	
Cap. Volts	
Starting amps.	

LOSSES	
Cond. stator	
rotor	
Iron tooth	
core	
surface	
pulsation	
Wind. & frict.	
Brush resist.	
frict.	
Total	
Efficiency %	

MAGNETIC CIRCUIT	
Area, gap/pole	
S. teeth	
S. core	
R. teeth	
R. core	
Phase volts	63.5
Flux/pole K.L.	
Density, gap	18.05
S. teeth	
core	
R. teeth	
core	
Gap length	.013
Slot open, S.	
R.	
Fring. stator	
rotor	
A.T. gap	
S. teeth	
core	
R. teeth	
core	
Total	
Amperes mag.	1.2
" gap.	

ROTOR DESIGN		
Equiv. N_1		
N_2		
Actual I_2/Phase		
Start. torq. %		
loss		
Rings ax. width	.50	.25
Rad. Depth	.375	.75
Material	Alum	
Conductivity %		
Resist. factor		
bars		
rings		
Equiv. R_2 at 75°		
Locked, X		
Z		
I		
%		
K.W. bars		
rings.		
KW/lb. bars		
rings		
Bar length		
Slip %		
Skew angle	1.5 RSP	
Brushes/Ring		
Brush Size		
Rotor Volts		
" Amps.		

RATING	
Horsepower	
Volts	110
Phases	3
Freq.	60
R.P.M.	3450
Poles	2
P.F.	
Amperes	
Frame	1452
Enclos.	DP
Time Rating	Cont
Temp. rise	40°C
Torque start. %	
max. %	
Design Letter	
Insul. Class	B
Type	
Similar to	
Supersedes	

~~Same~~ Half gap ollers sdy of A-4108

Designer YJN　　Date Dec 2/59　　DESIGN No. A-4108-2P

INDUCTION MOTOR — DESIGN SHEET

STATOR Lam No. E-12161 | **ROTOR** Lam No. Y-23412 | **NETT. WEIGHTS**

STATOR			ROTOR			NETT. WEIGHTS	
Diam. ext.	5.75	square	Diam. ext.	3.724		Stator Wdg.	3.50
int.	3.75		int.	.75		aux.	
Core stack.	2.75		Core stack.	2.75		Rotor cond.	.40
ducts			ducts			ring.	43
Stack. factor			Stack. factor			Stator teeth	
Iron	24 el		Iron			core	
No. of slots	36		No. of slots.	45		**MISCELLANEOUS DATA.**	
Core depth			Core depth				
Slot depth			Slot depth				
width			width			**AUX. WDG.**	
Wdg. area			Wdg. area			Capacitor	
Tooth width			Tooth width			Wdg. type	
Slot insul.	.020		Slot insul.			Slots per pole	
Wdg. type	Lap		Wdg. type	S.C.		Turns per coil	
connect.	Y		connect.			Conductor	
Slots/ph./pole	3		Slots/ph./pole			Coil pitch	
Turns/coil	21		Turns/coil			R. at 75°	
Cond./phase	504		Cond./phase			Rotor resist	
Cond. width	#19	HF	Cond. width	As slot		Locked, X	
depth			depth			Cap. X	
Factor space			Material	Alum		X.-Xc	
dist.			Conductivity %			Z	
pitch			Factor space			I	
Pitch coil	1-8		dist.			Cap. Volts	
slot			pitch			Starting amps.	
pole			Pitch coil			**LOSSES**	
Cond. length			slot			Cond. stator	
R at 75°	2.95		Cond. length			rotor	
volts at 75°			R at 75°			Iron tooth	
L.M.T.			volts at 75°			core	

MAGNETIC CIRCUIT			ROTOR DESIGN			LOSSES / RATING		
						surface	90	
Area, gap/pole			Equiv. N_1			pulsation		
S. teeth			N_2			Wind. & frict.	10	
S. core			Actual I_2/Phase			Brush resist.		
R. teeth			Start. torq. %			frict.		
			loss			Total		
R. core			Rings ax. width	.50	.25	Efficiency %	75.0	
Phase volts	127		Rad. Depth	.375	.75	**RATING**		
Flux/pole K.L.			Material	Alum		Horsepower	3/4	
Density, gap	35.3		Conductivity %			Volts	220	208
S. teeth			Resist. factor			Phases	3	
core			bars			Freq.	60	
R. teeth			rings			R.P.M.	1730	1726
			Equiv. R_2 at 75°			Poles	4	
core			Locked, X			P.F.	.785	
Gap length	.013		Z			Amperes	2.5	2.64
Slot open, S.			I			Frame	1452	
R.			%			Enclos.	D.P.	
Fring. stator			K.W. bars			Time Rating	Cont	
rotor			rings.			Temp. rise	40°C	
A.T. gap			KW/lb. bars			Torque start. %	350	
S. teeth			rings			max. %	350	
core			Bar length			Design Letter	A or B	
R. teeth			Slip %			Insul. Class		
			Skew angle	1.5 RSP		Type	86K	
core			Brushes/Ring			Similar to		
Total			Brush Size			Supersedes	3831	
Amperes mag.	1.6		Rotor Volts					
" gap.			" Amps.					

Designer F.G.W. Date May 2nd/57 **DESIGN No.** A-4108

INDUCTION MOTOR — DESIGN SHEET

STATOR Lam. No. E-12561			
Diam. ext.	5.75	square	
int.	3.75		
Core stack.	2.75		
ducts			
Stack. factor			
Iron	24 M36		
No. of slots	36		
Core depth			
Slot depth			
width			
Wdg. area			
Tooth width			
Slot insul.	.020		
Wdg. type	Lap		
connect.	Y		
Slots/ph./pole	2		
Turns/coil	31		
Cond./phase	744		
Cond. width	#21 HF		
depth			
Factor space			
dist.			
pitch			
Pitch coil	1-6		
slot			
pole			
Cond. length			
R at 75°		6.1	
volts at 75°			
L.M.T.	13.4		

MAGNETIC CIRCUIT			
Area, gap/pole			
S. teeth			
S. core			
R. teeth			
R. core			
Phase volts	127		
Flux/pole K.L.			
Density, gap	35000		
S. teeth			
core			
R. teeth			
core			
Gap length	.013		
Slot open, S.			
R.			
Fring. stator			
rotor			
A.T. gap			
S. teeth			
core			
R. teeth			
core			
Total			
Amperes mag.	1.72		
" gap.			

ROTOR Lam. No. Y-23412			
Diam. ext.	3.724		
int.	.75		
Core stack.	2.75		
ducts			
Stack. factor			
Iron			
No. of slots	45		
Core depth			
Slot depth			
width			
Wdg. area			
Tooth width			
Slot insul.			
Wdg. type	S.C.		
connect.			
Slots/ph./pole			
Turns/coil			
Cond./phase			
Cond. width / depth	As slot		
Material	Alum		
Conductivity %			
Factor space			
dist.			
pitch			
Pitch coil			
slot			
Cond. length			
R at 75°			
volts at 75°			

ROTOR DESIGN			
Equiv. N_1			
N_2			
Actual I_2/Phase			
Start. torq. %			
loss			
Rings ax. width	.50	.25	
Rad. Depth	.375	.75	
Material	Alum		
Conductivity %			
Resist. factor			
bars			
rings			
Equiv. R_2 at 75°			
Locked, X			
Z			
I			
%			
K.W. bars			
rings.			
KW/lb. bars			
rings			
Bar length			
Slip %			
Skew angle	1.5 R.S.P.		
Brushes/Ring			
Brush Size			
Rotor Volts			
" Amps.			

NET. WEIGHTS			
Stator Wdg.	3.1		
aux.			
Rotor cond.	.39		
ring.	.43		
Stator teeth			
core			

MISCELLANEOUS DATA.

AUX. WDG.			
Capacitor			
Wdg. type			
Slots per pole			
Turns per coil			
Conductor			
Coil pitch			
R. at 75°			
Rotor resist.			
Locked, X			
Cap. X			
X.-Xc			
Z			
I			
Cap. Volts			
Starting amps.			

LOSSES			
Cond. stator			
rotor			
Iron tooth			
core			
surface			
pulsation			
Wind. & frict.			
Brush resist.			
frict.			
Total			
Efficiency %	72.0		

RATING			
Horsepower	1/2		
Volts	220		
Phases	3		
Freq.	60		
R.P.M.	1140		
Poles	6		
P.F.	.62		
Amperes	2.0		
Frame	1452		
Enclos.	Drip		
Time Rating	Cont		
Temp. rise	40°C		
Torque start. %	275		
max. %	320		
Design Letter	B		
Insul. Class			
Type	B6K		
Similar to			
Supersedes			

Same gap density as A-4108

Designer HW .... Date Dec 2/59 .... DESIGN No. A-4108-6P

BIBLIOGRAPHY

1. Carpenter, C.J., "Surface Integral Methods of Calculating Forces on Magnetized Iron Parts", Proc. I.E.E., Vol. 107, Part C, No. 11, March 1960.

2. Steinmetz, C.P., Theory and Calculation of Electrical Apparatus, McGraw-Hill, New York, 1917.

3. Teare, B.R. Jr., "Theory of Hysteresis Motor Torque," A.I.E.E. Transactions, Vol. 59, pp. 907-912, 1940.

4. Roters, H.C., "The Hysteresis Motor. Advances Which Permit Economical Fractional Horse Power Ratings," A.I.E.E. Transactions, Vol. 66, pp. 1419-30, 1947.

5. Larionov, Mastayaev, Orbov, Panov, "Obshchie Voprosy Teorii Gizterezisnykli Electro Dvigatebi," Electrishevo, Vol. 78, No. 7, pp. 1-6, July 1958, Moscow.

6. Weaver, W. and Mason, M., The Electromagnetic Field, Dover Publications, New York, 1929.

7. Stratton, J.A., Electromagnetic Theory, McGraw-Hill, New York, 1941.

8. Betz, Burchan, and Ewing, Differential Equations with Applications, Harper & Brothers, New York, 1954.

9. The Arnold Engineering Company, The Magneteer, Vol. 2, No. 1, Marengo, Illinois, 1957.

10. Moullin, E.B., Principles of Electromagnetism, Oxford University Press, 1950.

11. Attwood, S.S., Electric & Magnetic Fields, Wiley, New York, 1949.

12. Christie, C., Electrical Engineering, McGraw-Hill, New York, 1952.

13. Fitzgerald and King, Electrical Machinery, McGraw-Hill, New York, 1952.

14. Attas, I., Noise in Induction Motors, A Thesis, McGill University, 1949.

15. Grey, Electrical Machine Design, McGraw-Hill, New York, 1926.

16. Moullin, E.B., Electromagnetic Principles of the Dynamo, Oxford University Press, 1955.

17. Roters, H.C., "The Hysteresis Motor," Electrical Engineering, Vol. 67, pp. 241-5, New York, 1948.

18. Spooner, T., Properties and Testing of Magnetic Materials, McGraw-Hill, New York, 1927.

19. Spooner, T., "Tooth Frequency Losses in Rotating Machines", Electrical Engineering, Vol. 40, p. 51, September 1921.

20. Brailsford, F., Magnetic Materials, Methuen Monograph, 1951

21. Carter, G.W., The Electromagnetic Field in its Engineering Aspects, Longmans, London, 1957.

22. Johnson, Analogue Computer Techniques, McGraw-Hill, New York, 1951.

23. Kunz, K.S., Numerical Analysis, McGraw-Hill, New York, 1957.

24. The Arnold Engineering Company, Arnold Magnetic Materials, Bulletin GC-106 C, Marengo, Illinois, 1957.

25. General Electric Company, Engineering Data on P-6 Magnetic Alloy, Edmore, Michigan, 1958.

26. The Indiana Steel Products Company, Ceramic Permanent Magnets, Bulletin No. 18, Valpariso, Indiana.

27. Veinott, C.G., Fractional Horse Power Electric Motors, McGraw-Hill, New York, 1948.

28. Kuhlman, J.H., Design of Electrical Apparatus, Wiley, New York, 1950.

29. Brailsford, F., "Rotational Hysteresis Loss in Sheet Steels", Proc. I.E.E., Vol. 83, p. 566, 1938.

30. Miner and Seastone, Handbook of Engineering Materials, Wiley, New York, 1955.

31. The International Nickel Co. Inc., Nickel Containing Alloys for Permanent Magnets, New York, 1955.